

Endothelial LATS2 is a suppressor of bone marrow fibrosis

Received: 13 April 2023

Accepted: 13 June 2024

Published online: 29 July 2024

 Check for updates

Kishor K. Sivaraj^{1,9}✉, Paul-Georg Majev^{1,9}, Backialakshmi Dharmalingam¹, Silke Schröder¹, Bella Banjanin², Martin Stehling³, Dagmar Zeuschner⁴, Alfred Nordheim^{5,6}, Rebekka K. Schneider^{2,7,8}✉ & Ralf H. Adams¹✉

Myelofibrosis and osteosclerosis are fibrotic diseases disrupting bone marrow function that occur in various leukemias but also in response to non-malignant alterations in hematopoietic cells. Here we show that endothelial cell-specific inactivation of the *Lats2* gene, encoding Hippo kinase large tumor suppressor kinase 2, or overexpression of the downstream effector YAP1 induce myofibroblast formation and lead to extensive fibrosis and osteosclerosis, which impair bone marrow function and cause extramedullary hematopoiesis in the spleen. Mechanistically, loss of LATS2 induces endothelial-to-mesenchymal transition, resulting in increased expression of extracellular matrix and secreted signaling molecules. Changes in endothelial cells involve increased expression of serum response factor target genes, and, strikingly, major aspects of the LATS2 mutant phenotype are rescued by inactivation of the *Srf* gene. These findings identify the endothelium as a driver of bone marrow fibrosis, which improves understanding of myelofibrotic and osteosclerotic diseases, for which drug therapies are currently lacking.

Fibrosis is associated with tissue injury, chronic inflammation and numerous other pathologies. In bone, fibrosis occurs in a variety of malignant and non-malignant disease conditions but also after acute or chronic exposure to radiation¹. In certain groups of rare blood cancers, namely in primary myelofibrosis and in myelodysplastic syndromes, bone marrow (BM) fibrosis is a risk factor and most prevalent in patients with advanced disease and poor prognosis². Excessive deposition of extracellular matrix (ECM) and tissue scarring contribute to impaired BM function, resulting in extramedullary hematopoiesis (EMH) and splenomegaly. Advanced bone fibrosis in human patients, but also in mouse models, can be accompanied by osteosclerosis, which manifests as irregular thickening of trabecular bone and abnormally elevated bone density^{3,4}.

Bone marrow mesenchymal stromal cells (BMSCs), especially cells expressing Leptin receptor (LepR) or the zinc finger protein Gli1, were previously shown to contribute to osteogenesis⁵⁻⁷. These BMSC populations are also critical mediators of myelofibrosis and osteosclerosis⁸⁻¹⁰. Expression of tumor necrosis factor α and JAK-STAT signaling were shown to be increased in pre-fibrotic BMSCs, whereas strong upregulation of TGF β signaling is predominant in overt fibrosis¹¹. Elevated numbers and aberrant properties of megakaryocytes are also associated with myeloproliferation, BM fibrosis and destruction of the hematopoietic microenvironment¹². Other alterations affecting hematopoietic cells, such as hypomorphic mutations in the transcription factor GATA1 or high expression of the glycoprotein hormone thrombopoietin (ThPO), cause myelofibrosis in mice¹³.

¹Department of Tissue Morphogenesis, Max Planck Institute for Molecular Biomedicine, Münster, Germany. ²Department of Developmental Biology, Erasmus University Medical Center, Rotterdam, The Netherlands. ³Flow Cytometry Unit, Max Planck Institute for Molecular Biomedicine, Münster, Germany. ⁴Electron Microscopy Unit, Max Planck Institute for Molecular Biomedicine, Münster, Germany. ⁵Department of Molecular Biology, Interfaculty Institute for Cell Biology, University of Tübingen, Tübingen, Germany. ⁶Leibniz Institute on Aging – Fritz Lipmann Institute, Jena, Germany. ⁷Onco Institute, Erasmus University Medical Center, Rotterdam, The Netherlands. ⁸Institute for Cell and Tumor Biology, Rheinisch-Westfälische Technische Hochschule (RWTH) Aachen University, Aachen, Germany. ⁹These authors contributed equally: Kishor K. Sivaraj, Paul-Georg Majev.

✉e-mail: kishor.kumar-sivaraj@mpi-muenster.mpg.de; reschneider@ukaachen.de; ralf.adams@mpi-muenster.mpg.de

Although the role of endothelial cells (ECs) in myelofibrosis remains little understood, it was previously shown that ECs of small vessels in BM and spleen of the JAK2-V617F knock-in mouse model, but also in patients with primary myelofibrosis, acquire the expression of mesenchymal markers, which is a hallmark of a process known as endothelial-to-mesenchymal transition (EndMT)¹⁴. ECs play critical roles in normal osteogenesis and hematopoiesis^{15,16}. In the metaphysis, specialized capillary ECs, termed type H because of high expression of the cell surface proteins CD31/Pecam1 and endomucin (EMCN), provide growth factor signals acting on perivascular osteoprogenitors and other osteoblast (OB) lineage cells expressing the transcription factors Runx2 and Osterix (OSX)¹⁶. The behavior and function of ECs is controlled by external growth factor signals but also by fluid shear stress, matrix stiffness and other mechanical signals¹⁷. The transcriptional coactivators YAP1 and TAZ, which are effectors in the Hippo signaling pathway, are capable of integrating a range of upstream signals to control cell proliferation, differentiation and tissue growth¹⁸. YAP1/TAZ interact in the nucleus with DNA-binding transcription factors, such as the TEA domain family members TEAD1–4, and thereby regulate gene expression¹⁹. Activation of the Hippo signaling cascade and large tumor suppressor homolog 1/2 (*Lats1/2*) kinase-mediated phosphorylation of YAP1/TAZ triggers exclusion of the transcriptional coactivators from the nucleus and promotes their proteolytic degradation²⁰. In the endothelium of most organs, YAP1/TAZ activity promotes angiogenic vessel growth, but, surprisingly, the two coactivators suppress EC proliferation and postnatal angiogenesis in bone²¹.

Here we demonstrate that EC-specific loss of the *Lats2* gene in ECs leads to extensive changes in the adult bone vasculature, EndMT and increased expression of ECM molecules and paracrine (also termed angiocrine) factors. These EC-specific changes promote the differentiation of metaphyseal BMSCs into myofibroblasts, resulting in bone fibrosis, osteosclerotic bone formation, impaired BM function and EMH. Loss of endothelial *Lats2* also impairs the formation of cartilage-resorbing septoclasts and results in the accumulation of chondrocytes (CHOs) in the mutant metaphysis. Mutant defects appear to be confined to the skeletal system, presumably due to compensation by LATS1 in other organs. These findings and the analysis of mouse models of myelofibrosis support that ECs play an instrumental role in bone fibrosis and need to be considered in disease etiology and in the context of therapeutic approaches.

Results

Endothelial LATS2 prevents bone vessel defects and fibrosis

We increased YAP1/TAZ protein stability in ECs by deleting the upstream negative regulator LATS2 during bone remodeling. For this purpose, the tamoxifen-inducible, EC-specific *Cdh5-CreERT2* transgene was introduced into animals carrying a loxP-flanked (floxed) version of the *Lats2* gene. Tamoxifen administration for 5 d in a row at the age of 4–5 weeks generated *Lats2* loss-of-function mutants (*Lats2*^{ΔEC}), which

were analyzed at the age of 12 weeks (Fig. 1a). Survival, body weight and the external appearance of *Lats2*^{ΔEC} mutant mice is normal, and YAP1/TAZ immunostaining in the bone vasculature is increased relative to littermate controls (Fig. 1b and Extended Data Fig. 1a). Endothelial expression of *Lats2*, which is most prominent in arteries and metaphyseal (type H) vessels, is strongly reduced in *Lats2*^{ΔEC} mutants both at the transcript and protein level (Extended Data Fig. 1b,c). The metaphysis of freshly isolated *Lats2*^{ΔEC} femurs appears whiteish, indicating a decrease of red marrow, and shows enhanced vascular leakage (Fig. 1c,d). The *Lats2*^{ΔEC} bone vasculature is substantially altered. Metaphyseal capillaries are very sparse, and an abnormally dense network of CD31⁺ ECs is visible in the transition zone connecting the metaphysis to the adjacent diaphysis (Fig. 1e–g and Extended Data Fig. 1d,e). Capillaries of the mutant metaphysis and transition zone show elevated CD31 immunostaining but decreased EMCN signal, have a small diameter or lack a lumen and express CAV1 (Caveolin 1), a caveolar protein that is highly abundant in control arterial ECs (Fig. 1f and Extended Data Fig. 1e). The *Lats2*^{ΔEC} chondro-osseous junction next to the growth plate is strongly disorganized, and Aggrecan⁺ hypertrophic CHOs occupy a large region of the metaphysis, which is confirmed by both Safranin O histological staining and Collagen X immunostaining (Fig. 1h,i and Extended Data Fig. 2a,b).

CHO resorption is mediated by vessel-associated FABP5⁺ septoclasts, which show high expression of metalloproteinases, including MMP9 (refs. 22,23). FABP5⁺ cells and MMP9 immunosignals are concentrated at the control chondro-osseous junction but are lost in *Lats2*^{ΔEC} mutant samples (Extended Data Fig. 2c). Another striking alteration in the *Lats2*^{ΔEC} mutant metaphysis is the strong upregulation of markers associated with tissue scarring and fibrosis, such as platelet-derived growth factor receptor β (PDGFRβ) and α-smooth muscle actin (αSMA⁺) (Fig. 1j,k and Extended Data Fig. 2d,e). Furthermore, AZAN trichrome and Reticulin histological staining, together with immunostaining for the ECM protein Collagen fibers, indicate widespread fibrosis in the *Lats2*^{ΔEC} metaphysis (Extended Data Fig. 2f,g).

To gain insight into the emergence of vascular defects and fibrosis in *Lats2*^{ΔEC} mutant bone, we analyzed samples at 8 weeks and 10 weeks of age. Increased perivascular αSMA expression is already visible at 8 weeks, and the disorganized area is further increased by 10 weeks (Extended Data Fig. 3a,b). Changes in the vasculature of the metaphysis and the transition zone bordering the diaphysis follow a similar timecourse (Extended Data Fig. 3c,d). Remarkably, fibrosis and vascular alterations in 12-week-old mutants are confined to bone, whereas no overt defects can be seen in kidney, lung, liver and heart sections (Extended Data Fig. 3e). Thus, loss of endothelial LATS2 leads to organ-specific defects in bone.

Osteosclerotic defects after loss of endothelial LATS2

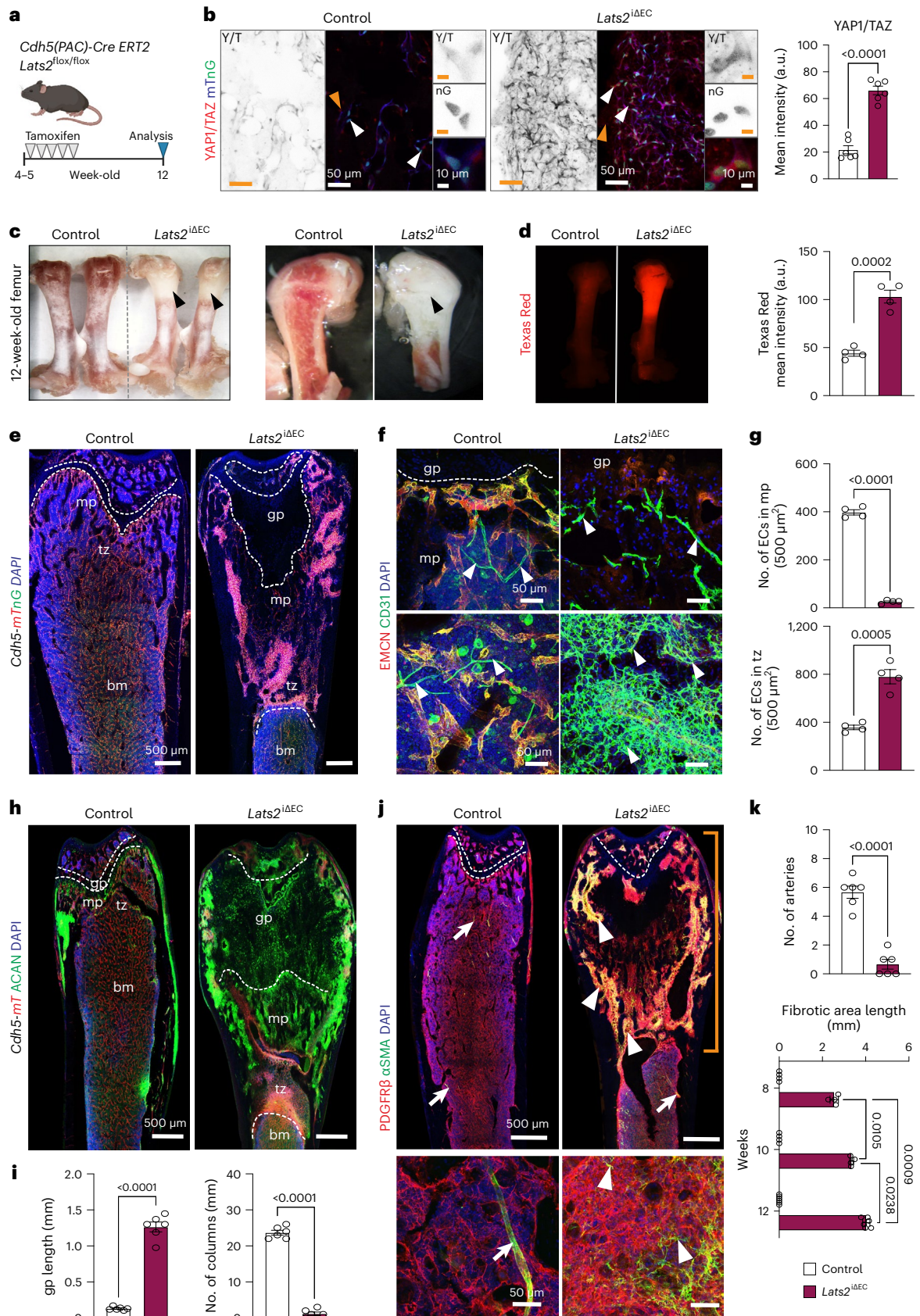
Bone fibrosis is known to cause the displacement of hematopoietic cells from BM, which leads to progressive splenomegaly due to

Fig. 1 | Endothelial *Lats2* controls bone homeostasis and fibrosis. **a**, Scheme showing tamoxifen-induced *Lats2* inactivation in ECs with *Cdh5-CreERT2* transgenic mice. **b**, Representative confocal images showing increased YAP1/TAZ immunostaining in *Lats2*^{ΔEC} mutant bones. Endothelial YAP1/TAZ expression and nuclear localization were quantified ($n = 6$) by the mean intensity (a.u.) on the right side. Data are presented as mean \pm s.e.m. P values, Mann–Whitney test (two-tailed). **c**, Freshly dissected 12-week-old control and *Lats2*^{ΔEC} mutant femurs (left) and longitudinal cross-section (right). Black arrowheads highlight pale areas. **d**, Microscopy images showing extravasation of Texas Red in control and *Lats2*^{ΔEC} mutant femur. On the right, the mean intensity (a.u.) of Texas Red is quantified ($n = 4$). Data are presented as mean \pm s.e.m. P values, Mann–Whitney test (two-tailed). **e**, Confocal tile scan longitudinal view of *Lats2*^{ΔEC} and control femur in *Cdh5-mTnG* background. ECs, red (dTomato) and green (nuclear H2B-GFP), DAPI (blue). **f,g**, Maximum intensity projections of EMCN⁺ (red) and CD31⁺ (green) vessels in the femoral metaphysis (mp) (top) and transition zone (tz)

(bottom). Note the abundance of mutant CD31⁺ EMCN⁺ ECs (**f**). Number of vessels and ECs is significantly reduced in the *Lats2*^{ΔEC} mp and increased in the tz area compared to control (**g**). Data ($n = 4$) are presented as mean \pm s.e.m. P values, Mann–Whitney test (two-tailed). **h,i**, Tile scan confocal image showing avascular region filled with Aggrecan⁺ (ACAN; green) chondrocytes in *Lats2*^{ΔEC} metaphysis (**h**). Quantification showing increased growth plate (gp) length and loss of type H vessel columns in *Lats2*^{ΔEC} mp ($n = 6$). Presented as mean \pm s.e.m. P values, Mann–Whitney test (two-tailed) (**i**). **j**, Tile scan confocal image and high-magnification image (below) showing widespread expression of PDGFRβ (red) and αSMA (green, arrowheads) in *Lats2*^{ΔEC} mutant femur. αSMA signal in control is confined to arterial SMCs. **k**, Quantification of arteries ($n = 6$) and length of fibrotic area (8-week-old and 10-week-old mice, $n = 4$; 12-week-old mice, $n = 6$). Mean \pm s.e.m. P values, Mann–Whitney test (two-tailed) and Tukey multiple comparison test (one-way ANOVA). n indicates the number of independent biological samples.

EMH²⁴. Analysis of *Lats2*^{ΔEC} peripheral blood shows an elevation of white blood cells, whereas red blood cells and platelets are similar to control (Extended Data Fig. 4a). In *Lats2*^{ΔEC} BM, total cellularity and Ter119⁺ erythrocytes and B220⁺ B lymphocytes are decreased, whereas

Lin⁻Sca-1⁺c-Kit⁺ (LSK) hematopoietic stem and progenitor cells (HSPCs) are not significantly altered (Fig. 2a and Extended Data Fig. 4b). CD41⁺ megakaryocytes are known to act as main drivers of myelofibrosis²⁴, but these cells are absent from the *Lats2*^{ΔEC} fibrotic area, and their



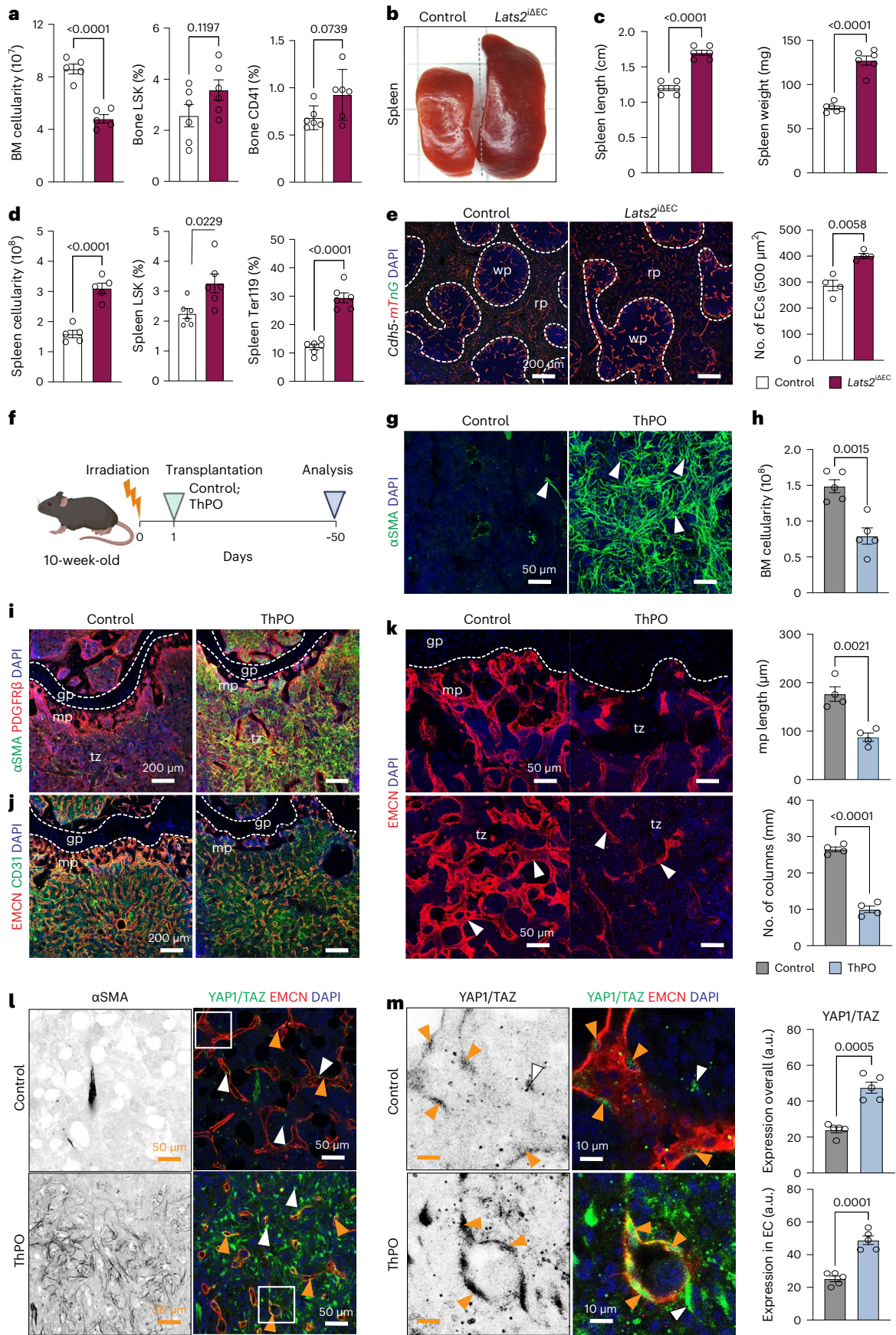


Fig. 2 | Loss of LATS2 promotes EMH. **a**, Quantification of BM cellularity and FACS analysis of LSK and CD41⁺ cell frequency ($n = 6$). Mean \pm s.e.m. P values, Mann–Whitney test (two-tailed). **b, c**, Images showing freshly dissected *Lats2*^{ΔEC} and control spleen (**b**) and quantification of spleen size and weight (**c**) ($n = 6$). Data are presented as mean \pm s.e.m. P values, Mann–Whitney test (two-tailed). **d**, Quantification of spleen cellularity and frequency of LSK and Ter119 cells ($n = 6$). Data are presented as mean \pm s.e.m. P values, Mann–Whitney test (two-tailed). **e**, Sections of control and *Lats2*^{ΔEC} spleens in *Cdh5-mTnG* reporter background. Red pulp (rp) and white pulp (wp) are indicated. Nuclei, DAPI (blue). Quantification showing increased EC number in *Lats2*^{ΔEC} mutant ($n = 4$). Data are shown as mean \pm s.e.m. P values, Mann–Whitney test (two-tailed). **f**, Scheme showing ThPO-induced BM fibrosis. **g**, Representative confocal images showing α SMA (green) immunostaining in ThPO and control bone. Nuclei, DAPI (blue). **h**, Quantification of BM cellularity of control and ThPO mice ($n = 5$). Data are

presented as mean \pm s.e.m. P values, Mann–Whitney test (two-tailed). **i, j**, Representative confocal images showing increase of metaphyseal α SMA signal (**i**) and reduction of EMCN⁺ CD31⁺ vessels (**j**) in ThPO femur relative to control. **k**, EMCN⁺ ECs (red) in metaphysis (mp) (top) and diaphysis (dp) (bottom). Nuclei, DAPI (blue). Graphs on the right show decreased mp length and vessel columns after ThPO ($n = 4$). Data are shown as mean \pm s.e.m. P values, Mann–Whitney test (two-tailed). **l, m**, Representative single optical confocal images showing increased expression of α SMA (gray) and YAP1/TAZ (green) in EMCN (red) ECs (orange arrowheads) in ThPO bone (**l**). Cropped zoomed-in image displays YAP1/TAZ nuclear (DAPI, blue) localization in ECs (**m**). Quantification shows increase of overall and EC-specific Yap1/TAZ immunosignal in ThPO bones ($n = 5$). Data are shown as mean \pm s.e.m. P values, Mann–Whitney test (two-tailed). n indicates the number of independent biological samples.

total number is not significantly altered in mutant femurs due to their presence in the diaphyseal BM (Fig. 2a and Extended Data Fig. 4c,d). Consistent with EMH, *Lats2*^{ΔEC} mutants show increased spleen volume and cellularity together with an increase in splenic HSPCs and Ter119⁺ cells, whereas the fractions of CD45⁺ leukocytes and B220⁺ cells are reduced (Fig. 2b–d and Extended Data Fig. 4e). In spleen sections, the area of red pulp is increased relative to white pulp, a feature of EMH (Fig. 2e and Extended Data Fig. 4f,g). These alterations are likely to be secondary to the defects in *Lats2*^{ΔEC} BM, as YAP1/TAZ immunostaining in splenic vessels is not increased (Extended Data Fig. 4h). Thus, *Lats2*^{ΔEC} mutants display splenomegaly, BM fibrosis and impaired BM function, resembling key features of myelofibrosis.

The etiology of myelofibrosis in human subjects is poorly understood, but previous work established that BM fibrosis in mice can be induced by overexpressing ThPO from hematopoietic cells, which results in the expansion of megakaryocytes, elevated expression of platelet-derived growth factor and transforming growth factor β and the activation of mesenchymal stromal cells^{10,25}. ThPO overexpression in HSPCs first leads to leukocytosis and thrombocytosis and, over time, with onset of fibrosis, reduced hemoglobin and erythrocyte counts (Fig. 2f and Extended Data Fig. 5a). The ThPO overexpression model mirrors aspects of the *Lats2*^{ΔEC} phenotype: increased and widespread α SMA immunostaining reflecting fibrosis, a general loss of cellularity in bone as well as an increase in spleen weight (Fig. 2g–i and Extended Data Fig. 5b,d). Remarkably, ThPO overexpression also induces a marked reduction of metaphyseal type H vessels and lowers endothelial EMCN expression (Fig. 2j,k and Extended Data Fig. 5c). Consistent with the loss of type H vessels, perivascular OSX⁺ OB lineage cells are strongly reduced in long bones of ThPO-overexpressing mice (Extended Data Fig. 5e). Strikingly, ThPO induces a strong increase in YAP1/TAZ immunostaining in fibrotic BM (Extended Data Fig. 5f), but it also significantly enhances YAP1/TAZ in ECs relative to control (Fig. 2l,m). Somatic activating mutations (such as W515L) in the transmembrane domain of the ThPO receptor, encoded by the *MPL* gene, are a driver of primary myelofibrosis in humans. Transplantation of

MPL^{W515L}-expressing hematopoietic cells can reproduce major features of the disease, including splenomegaly and extramedullary hematopoiesis, in mice²⁶. In the MPL^{W515L} model, fibrosis is accompanied by widespread upregulation of α SMA (Extended Data Fig. 5g,h). Strikingly, the EMCN⁺ BM vasculature of these mice is significantly reduced, and YAP1/TAZ immunostaining in vessels is upregulated (Extended Data Fig. 5h,i). These data show that vascular alterations and upregulation of YAP1/TAZ are a common feature in two established models of myelofibrosis.

LATS2 and the related LATS1 kinase phosphorylate YAP1 and TAZ, which limits the activity of the two transcriptional coregulators due to cytoplasmic retention and proteasomal degradation. To directly address the role of YAP1 and TAZ, we generated tamoxifen-inducible, EC-specific loss-of-function double mutant mice (*Yap1/Taz*^{ΔEC}), which were given tamoxifen at the age of 4–5 weeks before analysis at 12 weeks. In contrast to the enhanced developmental angiogenesis in postnatal *Yap1/Taz*^{ΔEC} bone²¹, adult mutants display a normal organization of the bone vasculature and also lack alterations in PDGFR β and α SMA expression (Fig. 3a–c). Overexpression of stabilized YAP1 (YAP1^{S112A}) in ECs, however, causes the formation of sclerotic lesions, vascular impairment and the appearance of an EMCN-deficient endothelial network in the metaphysis of the resulting *YapK*^{fEC} gain-of-function mutants (Fig. 3d–f). Key defects observed in *Lats2*^{ΔEC} mutants, such as expansion of chondrocytes and widespread expression of PDGFR β and α SMA, are also observed in *YapK*^{fEC} animals (Fig. 3g–i).

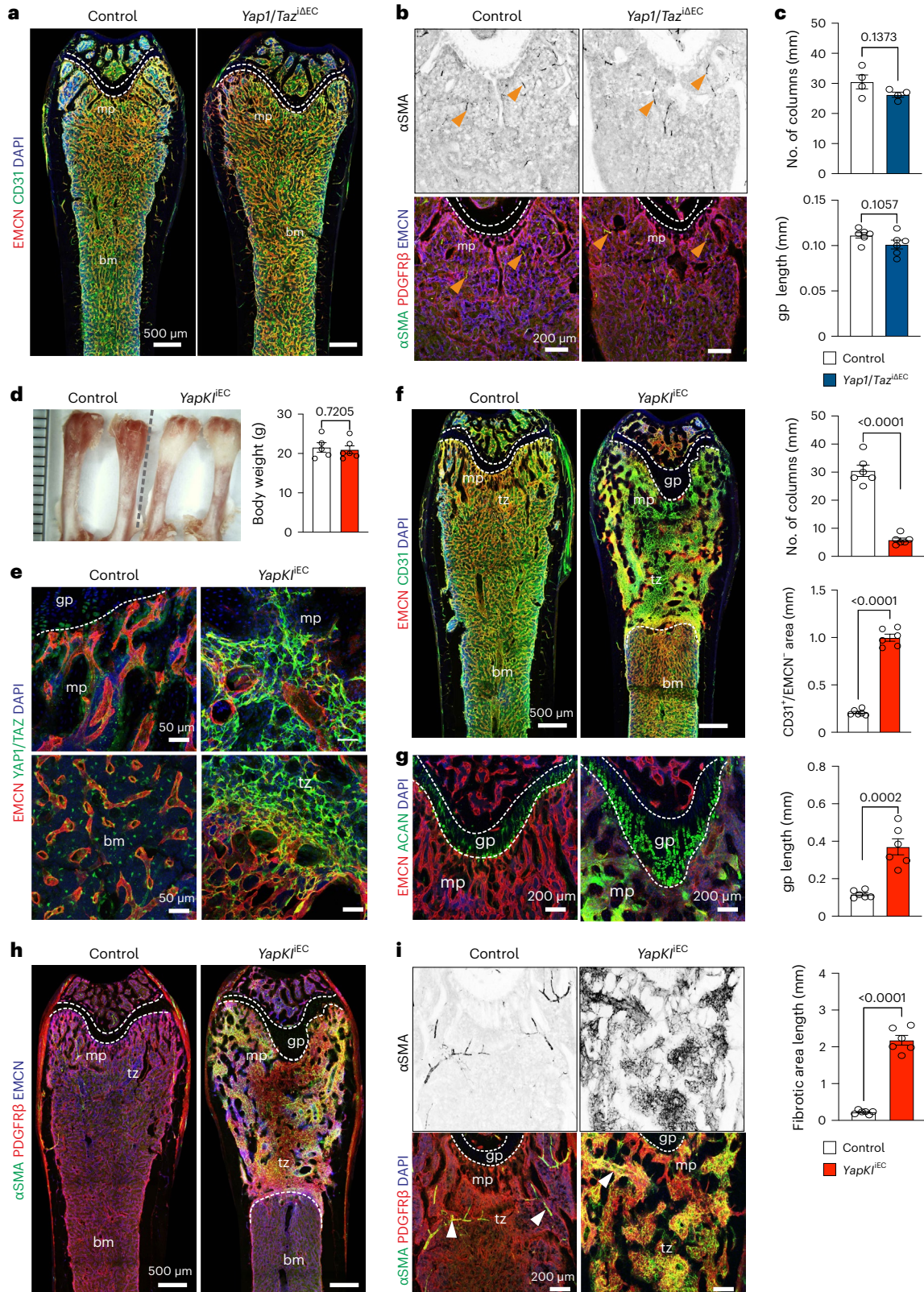
Previous work showed that metaphyseal type H capillaries are associated with osteoprogenitor cells and actively promote osteogenesis¹⁶. OSX⁺ cells and RUNX2⁺ osteoprogenitors are strongly reduced in the *Lats2*^{ΔEC} metaphysis in regions that have lost capillaries. In contrast, OB lineage cells are enriched around the dense but disorganized endothelial network in the mutant transition zone (Fig. 4a,b). Analysis of bone remodeling using the Calcein Green and Alzarin Red double labeling approach (Methods) shows decreased osteogenesis and resorption in *Lats2*^{ΔEC} long bone (Fig. 4c). Vacuolar ATPase (vATPase)-expressing osteoclasts are decreased in the avascular metaphysis and elevated in

Fig. 3 | Overexpression of a stabilized Yap1 in ECs promotes BM fibrosis. **a**, Tile scan confocal overview images of EMCN (red) and CD31 (green) immunostained vasculature in control and *Yap1/Taz*^{ΔEC} compound mutant femur. Metaphysis (mp), bone marrow (bm) and growth plate (gp) (dashed lines) are indicated. **b, c**, Representative confocal image of femoral α SMA⁺ (green) smooth muscle cells covering arteries (arrows) (above). EMCN⁺ (blue) blood vessels and PDGFR β ⁺ cells (red) in *Yap1/Taz*^{ΔEC} mutant and littermate control (below). Metaphyseal vessel columns and gp are not altered in *Yap1/Taz*^{ΔEC} bone (**c**) ($n = 4, 6$). Data are shown as mean \pm s.e.m. P values, Mann–Whitney test (two-tailed). **d**, Freshly dissected 12-week-old *YapK*^{fEC} gain-of-function and control femurs. Quantitative analysis of *YapK*^{fEC} and littermate control body weight ($n = 5$). Data are shown as mean \pm s.e.m. P values, Mann–Whitney test (two-tailed). **e**, Representative confocal images showing increased YAP1/TAZ (green) expression in *YapK*^{fEC} blood vessels (EMCN⁺, red) relative to control. **f**, Tile scan longitudinal view

of EMCN and CD31 immunostaining in femur sections. Quantification shows decrease in number of vessel columns and increase in CD31⁺/EMCN⁺ vascular area in *YapK*^{fEC} mutant ($n = 6$). Data are shown as mean \pm s.e.m. P values, Mann–Whitney test (two-tailed). **g**, Representative confocal images showing increase in Aggrecan⁺ (ACAN⁺) chondrocytes in *YapK*^{fEC} femur. Graph shows increased size of gp relative to control ($n = 6$). Data are shown as mean \pm s.e.m. P values, Mann–Whitney test (two-tailed). **h, i**, Tile scan confocal longitudinal view of PDGFR β ⁺ (red) and α SMA⁺ (green) cells. α SMA in control sections is largely confined to arterial smooth muscle cells (**h**). High-magnification images of α SMA⁺ (gray) fibrotic area is shown on the top right. gp (dashed line), metaphysis (mp) and transition zone (tz) to BM are indicated (**i**) ($n = 6$). Data are shown as mean \pm s.e.m. P values, Mann–Whitney test (two-tailed). n indicates the number of independent biological samples.

the mutant transition zone (Extended Data Fig. 6a). Microcomputed tomography (μ CT) shows highly increased trabecular bone volume, quantity and thickness in *Lats2* ^{Δ EC} mutant femurs, whereas cortical bone thickness is not changed (Fig. 4d and Extended Data Fig. 6b,c). Supporting that the role of LATS2 in bone endothelium involves the modulation of YAP1/TAZ, *YapKl*^{IEC} gain-of-function increases the number of osteoprogenitors, alters the distribution of osteoclasts and leads

to sclerotic mineralization (Fig. 4e–g). In contrast, adult *Yap1/Taz* ^{Δ EC} loss-of-function mutants show a modest decrease of OSX⁺ osteoprogenitors, whereas bone mineralization is unaffected (Extended Data Fig. 6d,e). These findings indicate that YAP1/TAZ levels are normally kept low in the adolescent/adult bone endothelium so that EC-specific overexpression of YAP1 or loss of LATS2 severely impair bone remodeling and homeostasis.



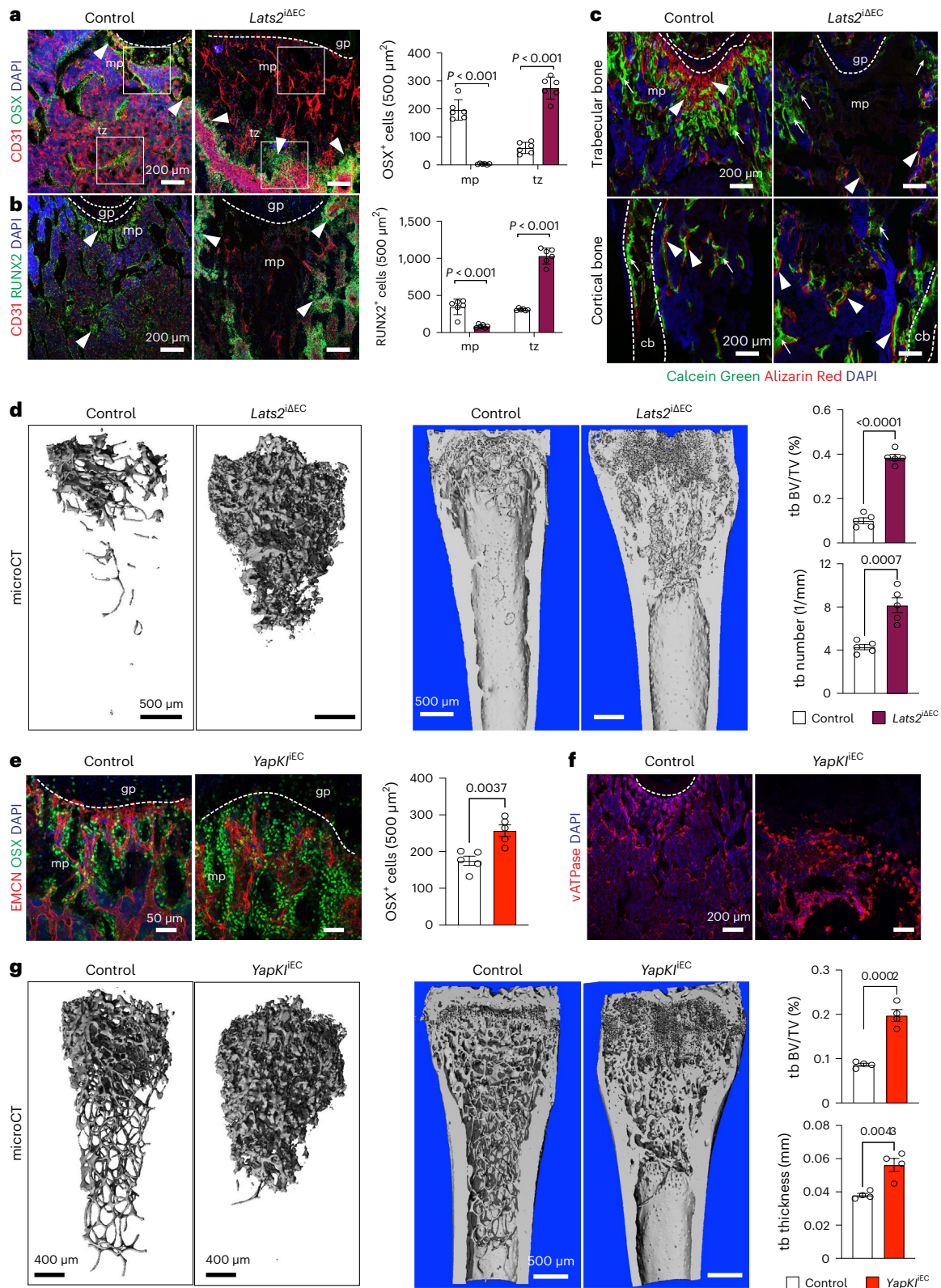


Fig. 4 | Endothelial Hippo signaling controls osteosclerosis. **a,b**, Representative confocal images showing OSX⁺ cells (**a**) and RUNX2⁺ osteoprogenitors (**b**) (arrowheads) in 12-week-old *Lats2*^{ΔEC} femur and littermate control (*n* = 6). Data are shown as mean ± s.e.m. *P* values, Mann–Whitney test (two-tailed). **c**, Representative confocal image showing double labeling with Calcein Green and Alizarin Red in metaphysis (mp) (top) and border to diaphysis (dp) (bottom) in control and *Lats2*^{ΔEC} femur. Arrow highlights Calcein Green deposition, and arrowheads show double labeling of deposition/resorption. **d**, Representative μCT images of *Lats2*^{ΔEC} and control femoral trabecular bone

(tb). Quantitative analysis of tb volume (bone volume/total volume (BV/TV)) and number are shown on the right (*n* = 5). Data are shown as mean ± s.e.m. *P* values, Mann–Whitney test (two-tailed). **e,f**, Representative confocal image showing OSX⁺ cells in control and *YapK1*^{ΔEC} femoral metaphysis (*n* = 5). Data are shown as mean ± s.e.m. *P* values, Mann–Whitney test (two-tailed) (**e**). vATPase⁺ osteoclasts (red) are reduced in the *YapK1*^{ΔEC} fibrotic area (**f**). **g**, Representative μCT images of tb in control and *YapK1*^{ΔEC} femur. Quantitative analysis of tb volume (BV/TV) and number (*n* = 4). Data are presented as mean ± s.e.m. *P* values, Mann–Whitney test (two-tailed). *n* indicates the number of independent biological samples.

LATS2 deletion induces EndMT

To determine stromal cell heterogeneity, fate specification and cellular crosstalk in *Lats2*^{ΔEC} mutant and littermate control long bone, we performed droplet-based single-cell RNA sequencing (scRNA-seq) of non-hematopoietic bone stromal cells with the 10x Chromium platform. We obtained a total of 20,184 cells after removing doublets and residual hematopoietic cells from scRNA-seq experiments of control and *Lats2*^{ΔEC} mutants with two biological replicates each. Based on the expression of known marker genes, we identified six primary cell types: ECs, BMSCs, OBs, smooth muscle cells (SMCs), CHOs and fibroblasts as well as their subpopulations. BMSC numbers are decreased and CHO and SMC numbers are increased in *Lats2*^{ΔEC} mutants (Fig. 5a–c and Extended Data Fig. 7a–c). Within the EC cluster, metaphyseal (type H) ECs (mpECs, Ramp3⁺), bone marrow (type L) ECs (bmECs, Stab2⁺), arteriole-like ECs (alECs, Fmo2⁺) and arterial ECs (aECs, Gja4⁺) can be readily identified (Extended Data Fig. 7d–f). When compared to controls, *Lats2*^{ΔEC} ECs exhibit numerous downregulated but also strongly upregulated differentially expressed genes (DEGs) (Extended Data Fig. 7g). *Lats2*^{ΔEC} mutant mpEC and aEC subpopulations show particularly large numbers of upregulated genes (Fig. 5d). Expression of the YAP1/TAZ-controlled target genes *Ccn1* (encoding cysteine-rich angiogenic inducer 61 (CYR61)), *Ccn2* (connective tissue growth factor (CTGF)), *Angpt1* (angiopoietin 1) and *Thbs1* (thrombospondin 1) is strongly increased (Extended Data Fig. 7h). Surprisingly, genes typical for mesenchymal cells and fibroblasts are also strongly upregulated in *Lats2*^{ΔEC} mpECs. The differential expression of a subset of these genes, including *Vim* (encoding the intermediate filament protein vimentin), *Tagln* (smooth muscle 22α, SM22α), *Fn1* (fibronectin 1), *Thbs1* and *Angpt2* is confirmed by immunostaining of the corresponding gene products in bone sections (Fig. 5e,f and Extended Data Fig. 8a). Additionally, we noticed that *Lats2*^{ΔEC} mutant type H ECs (mpECs) show expression of gene signatures associated with ECM, cell–matrix adhesion and actin cytoskeleton (Fig. 5g and Extended Data Fig. 8b). Furthermore, immunostaining of two critical downstream regulators controlling cell–matrix interactions, active integrin β1 and phosphorylated focal adhesion kinase (FAK), is strongly increased (Extended Data Fig. 8b). Ultrastructural analysis by transmission electron microscopy confirms the profoundly increased deposition of matrix components in the *Lats2*^{ΔEC} metaphysis and pronounced actin fibers in mutant ECs (Extended Data Fig. 8c). Genetic lineage tracing supports that *Lats2*^{ΔEC} ECs are not fully converted into mesenchymal stromal cells (Extended Data Fig. 8d) but acquire a mesenchymal cell-like phenotype through EndMT, including the expression of typical mesenchymal markers and elevated cell–matrix interactions.

Endothelial signals control myofibroblast generation

Previous research revealed that *Lepr-Cre*⁺ and *Gli1*⁺ mesenchymal stromal cells give rise to myofibroblasts during hematopoietic cell-induced myelofibrosis^{9,10}. As the exact nature of the processes leading to bone fibrosis is incompletely understood, we analyzed gene expression changes in different cell populations. We noted that transcriptional alterations in *Lats2*^{ΔEC} mpMSCs (Osteo-CAR) cells are more extensive than those seen in diaphyseal mesenchymal stromal

cells (dpMSCs; Adipo-CAR cells) or OBs (Fig. 6a). In the CHO cluster, pre-hypertrophic chondrocytes (PHCHOs) and hypertrophic chondrocytes (HCHOs) show the largest number of DEGs (Fig. 6b,c). We also noted a strong enrichment of *Myh11*⁺ cells in the *Lats2*^{ΔEC} SMC cluster, which show increased expression of markers associated with fibrosis and are likely to represent myofibroblasts (Fig. 6d–f). Analysis of the same scRNA-seq data also shows a pronounced shift within the *Lats2*^{ΔEC} mpMSC subcluster, indicative of altered gene expression relative to control (Fig. 6d). Pseudotime²⁷ and partition-based graph abstraction (PAGA)²⁸ analysis of the *Lats2*^{ΔEC} scRNA-seq data suggest a potential differentiation trajectory from mpMSCs to *Myh11*⁺ cells in the SMC cluster (Fig. 7a–d). Although *Gli1* expression is most prominent in the mpMSC/Osteo-CAR subcluster, *Acta2* transcripts (encoding αSMA) are abundant in *Myh11*⁺ SMCs and strongly upregulated in *Lats2*^{ΔEC} *Myh11*⁺ SMCs/myofibroblasts (Fig. 7e). Consistent with previous studies highlighting the role of *Gli1*⁺ cells as a source of myofibroblasts in bone fibrosis¹⁰, *Gli1-CreERT2*-mediated recombination of a Cre reporter allele labels vessel-associated BMSCs in the 12-week-old metaphysis, namely mpMSC/Osteo-CAR cells (Fig. 7f,g).

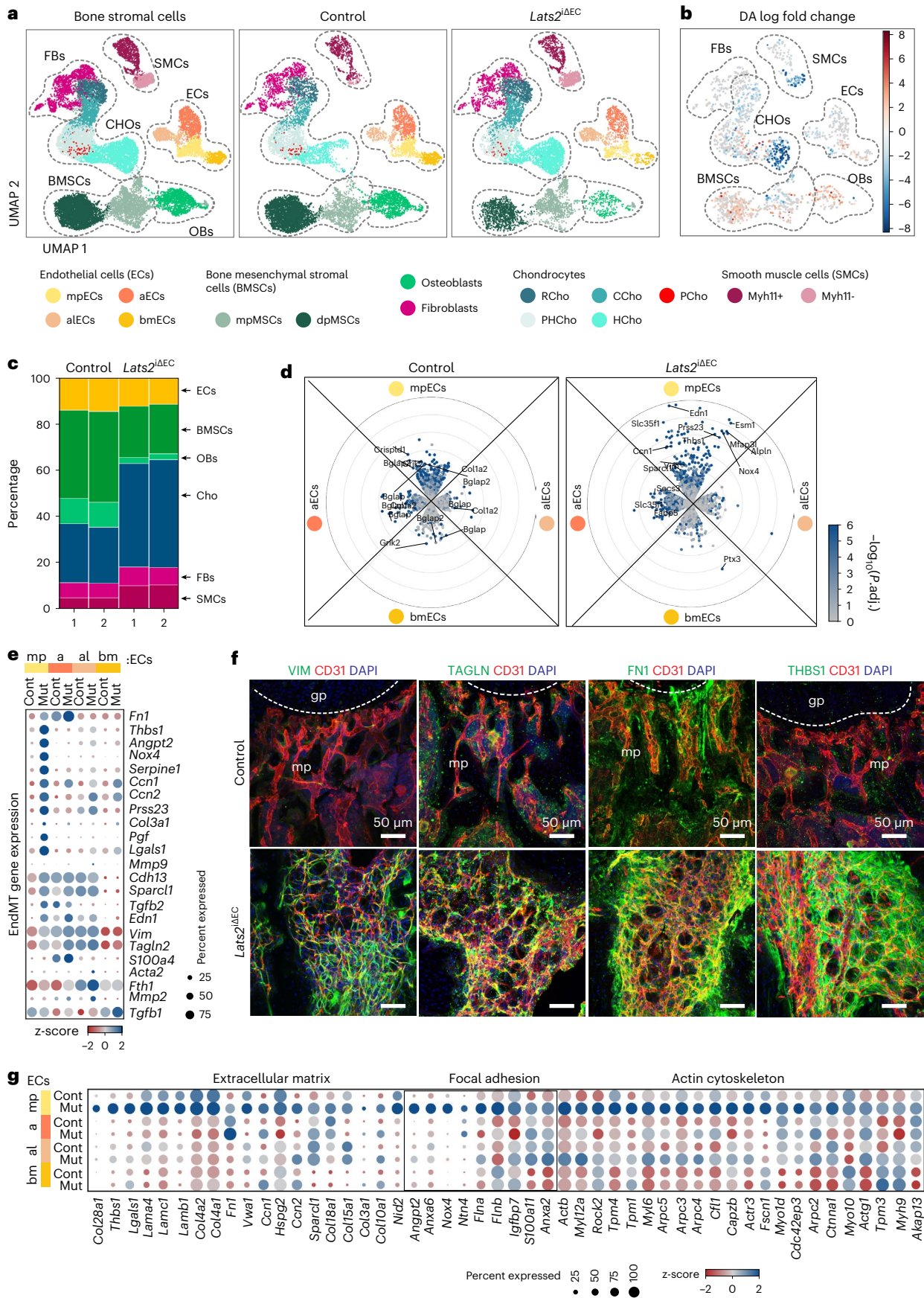
Next, we sought to understand which EC-derived signals might lead to the conversion of mpMSC/Osteo-CAR cells into myofibroblasts and the emergence of fibrosis in the *Lats2*^{ΔEC} metaphysis. To identify potential ligand–receptor interactions (LRIs), we employed a newly developed approach (Methods) similar to CellPhoneDB²⁹. *Lats2*^{ΔEC} mutant mpECs show substantially increased paracrine signaling capability compared to other EC subtypes, reflected by strongly elevated expression of secreted molecules relative to control (Extended Data Fig. 9a). In turn, many of the respective receptors for these EC-derived ligands are expressed or even elevated in other cell types in *Lats2*^{ΔEC} bone (Fig. 8a,b and Extended Data Fig. 9b). Specifically, genes involved in cell–matrix interactions (*Thbs1*, *Fn1*, *Col4a1*, *Col18a1* and *Plau*), the glycoprotein von Willebrand factor (*Vwf*) and secreted signaling molecules, such as adrenomedullin (*Adm*), apelin (*Apn*), angiopoietin 2 (*Angpt2*) and endothelin 1 (*Edn1*), are upregulated in *Lats2*^{ΔEC} mutant mpECs (Extended Data Fig. 9c). The corresponding receptors are expressed by multiple cell populations but are frequently found in mpMSCs and the *Myh11*⁺ SMC subcluster (Extended Data Fig. 9c,d). Treatment of cultured BMSCs with recombinant endothelin 1 can increase the expression of fibrosis markers similar to TGFβ1, whereas adrenomedullin has no significant effect under the same conditions (Extended Data Fig. 9e). Based on these results, we propose that loss of LATS2 in ECs is sufficient to initiate bone fibrosis through the upregulation of EC-derived secreted molecules.

YAP1/TAZ control EC plasticity through serum response factor

To gain insight into the mechanism controlling EndMT in *Lats2*^{ΔEC} mutants, we used iRegulon³⁰ to examine which transcription factors are likely regulators of the gene expression changes in mpECs. Serum response factor (SRF) is the top hit in this analysis, and SRF target genes are upregulated in *Lats2*^{ΔEC} mpECs (Fig. 9a,b). Further arguing for a potential role of SRF, transcript and protein are highly increased in mutant mpECs relative to control (Fig. 9c–e). *Srf* inactivation in

Fig. 5 | EndMT after loss of LATS2. a, b, UMAP plots showing merged (left) and separated control and *Lats2*^{ΔEC} mutant (right) bone stromal cells color-coded by cell type (a). Changes in cellular abundance (differential abundance (DA)) as calculated with milopy. Negative values indicate increased abundance in *Lats2*^{ΔEC} mutant (b). Metaphyseal ECs (mpECs), arteriole-like ECs (alECs), arterial ECs (aECs), metaphyseal MSCs (mpMSCs), Osteo-CAR), diaphyseal MSCs (dpMSCs, Adipo-CAR), resting chondrocytes (RCHOs), columnar chondrocytes (CCHOs), proliferating chondrocytes (PCHOs), pre-hypertrophic chondrocytes (PHCHOs), hypertrophic chondrocytes (HCHOs) as well as *Myh11*⁺ and *Myh11*[−] SMCs are indicated. **c**, Bar graph displaying percentage of each main bone stromal cell type. **d**, Radial expression plot (Methods) showing DGE of control and *Lats2*^{ΔEC}

EC subclusters. *y* axis shows log₂ fold expression changes; color scale represents the adjusted *P* values. **e**, Dot plot for normalized and averaged expression indicates high expression of mesenchymal markers and fibroblast genes in *Lats2*^{ΔEC} mpECs. *z*-scaled per row. **f**, Immunostaining showing high levels of Vimentin (VIM), Transgelin (TAGLN), Fibronectin 1 (FN1) and Thrombospondin 1 (THBS1) in *Lats2*^{ΔEC} metaphysis (mp). Control growth plate (gp) is marked by the dashed line. ECs (CD31, red) and nuclei (DAPI, blue) are labeled. **g**, Row-wise *z*-scaled normalized expression values of ECM, focal adhesion and actin cytoskeleton genes in *Lats2*^{ΔEC} mutant and control EC populations. FB, fibroblast.



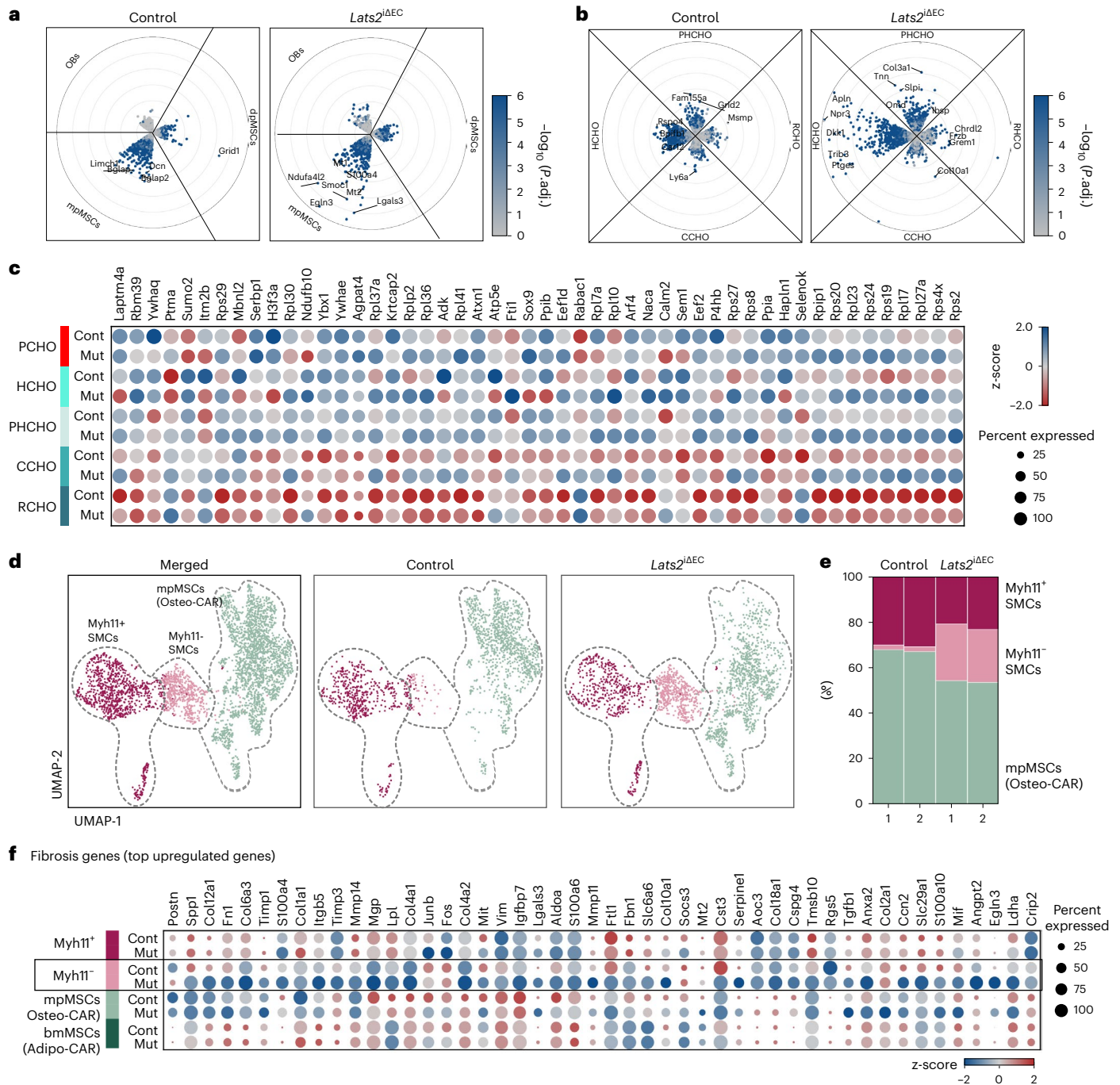


Fig. 6 | EC-derived signals control mpMSCs and CHOs. a–c, Radial expression plot (Methods) of BMSC/OB subsets, showing that most significant differences in regulation between conditions occur in mpMSCs (a). Within the CHO subset, most differences between conditions are confined to HCHOs. Proliferating CHOs are not shown, as number was less than 50 (b). Genes significantly differentially expressed ($P_{adj} \leq 0.01$, $\log_2 FC < 0$, frac. expressed ≥ 0.2) between control (Cont) and mutant (Mut) in at least one CHO sub-identity (c). **d, e,** UMAP visualization of mpMSC and SMC subclusters showing all cells (left) or split by genotype (right) (d). Percentage of cells in each cell type per sample is shown. Note increase in *Lats2^{ΔEC}* Myh11⁻ SMCs representing myofibroblasts (e). **f,** Row-wise z-scaled normalized expression values of fibrosis genes in Myh11⁻ cells relative to mpMSCs, dpMSCs and Myh11⁺ SMCs.

and mutant (Mut) in at least one CHO sub-identity (c). **d, e,** UMAP visualization of mpMSC and SMC subclusters showing all cells (left) or split by genotype (right) (d). Percentage of cells in each cell type per sample is shown. Note increase in *Lats2^{ΔEC}* Myh11⁻ SMCs representing myofibroblasts (e). **f,** Row-wise z-scaled normalized expression values of fibrosis genes in Myh11⁻ cells relative to mpMSCs, dpMSCs and Myh11⁺ SMCs.

ECs (*Srf^{ΔEC}*) alone has no significant effect on the bone vasculature, tissue organization, markers of fibrosis, growth plate size or mineralized bone, but CD31⁺/EMCN⁻ vessels, representing arteries/arterioles, are slightly reduced, and OSX⁺ cells are increased (Extended Data Fig. 10a–e). In EC-specific *Lats2* and *Srf* compound mutants (*Lats2 Srf^{ΔEC}*) generated with the same tamoxifen administration regime described earlier, the lack of SRF largely restores the normal organization of metaphyseal vasculature and EMCN expression

in the *Lats2^{ΔEC}* background (Fig. 9f and Extended Data Fig. 10f–h). Vascular normalization is accompanied by the restoration of normal growth plate size and bone mineralization as well as reduction of PDGFR β and α SMA immunostaining in *Lats2 Srf^{ΔEC}* compound mutants (Fig. 9g,h and Extended Data Fig. 10i,j). The sum of these data shows that LATS2 limits YAP1/TAZ expression in bone ECs to prevent EndMT and SRF-mediated processes, leading to fibrosis and osteosclerotic defects (Extended Data Fig. 10k).

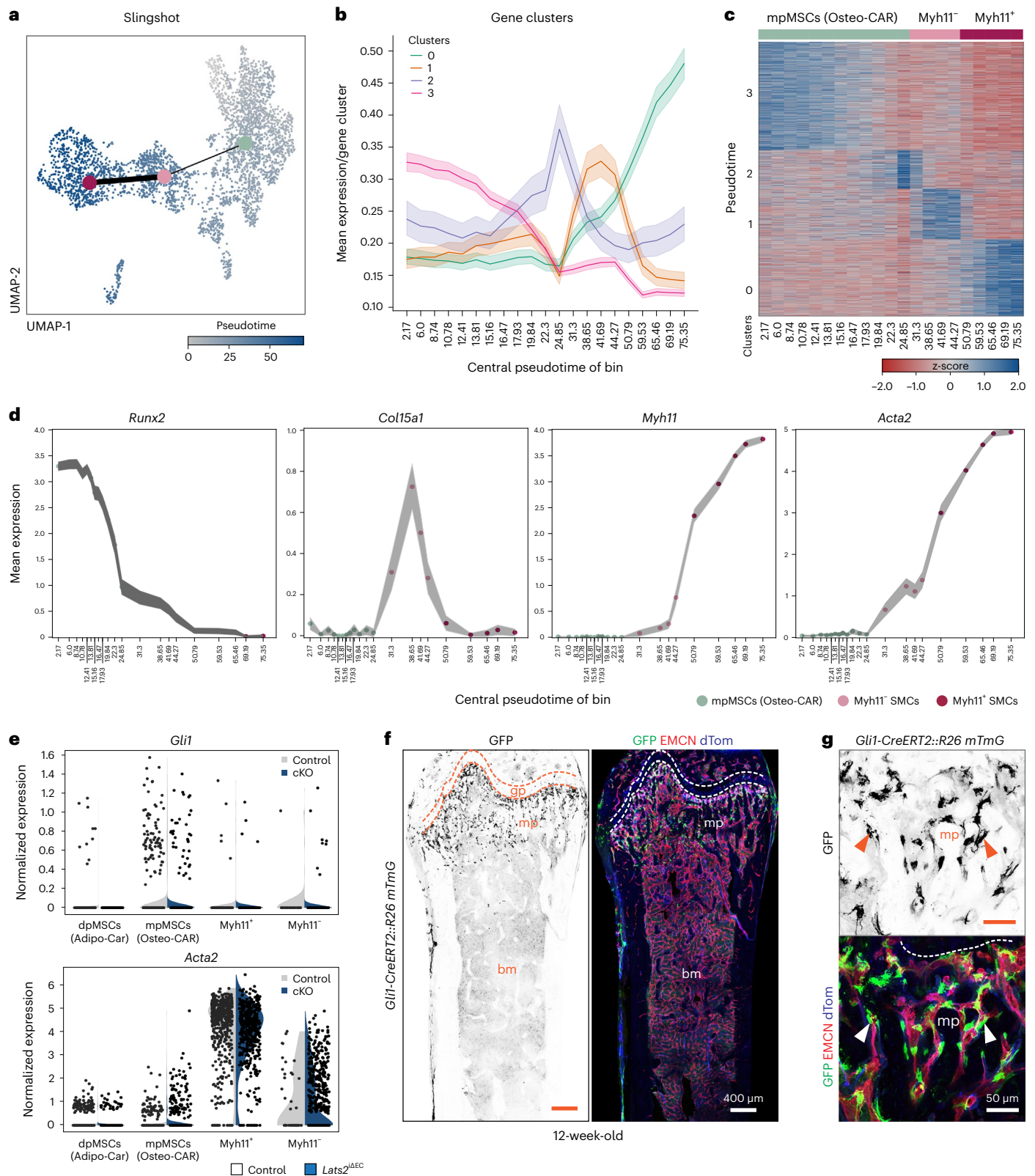


Fig. 7 | Conversion of mpMSCs into myofibroblasts. **a–c**, UMAP plot colored by slingshot pseudotime. Centroid dots show cell type identity, and connecting lines indicate cell type connectivities calculated by PAGA (**a**). Visualization of mean expression in gene clusters as determined by Leiden clustering genes along the slingshot pseudotime trajectory; filled areas show 95% confidence interval (**b**). Heatmap of these gene clusters showing gene expression changes across pseudotime (**c**). **d**, Selected marker genes showing continuous gene expression changes across the pseudotime trajectory from mpMSC to Myh11⁺

SMC. Normalized expression counts averaged per pseudotime bin are shown; filled areas show 95% confidence interval. **e**, Violin plots showing *Gli1* and *Acta2* expression in dpMSCs/Adipo-CAR cells, mpMSCs/Osteo-CAR cells as well as Myh11⁻ and Myh11⁺ SMCs of *Lats2*^{ΔEC} mutants relative to control. **f, g**, Longitudinal tile scan confocal images showing *Gli1-CreERT2*-labeled cells (green) in the metaphysis (**f**). High-magnification images confirm perivascular location of GFP⁺ cells (**g**). EMCN (red) and dTomato (blue).

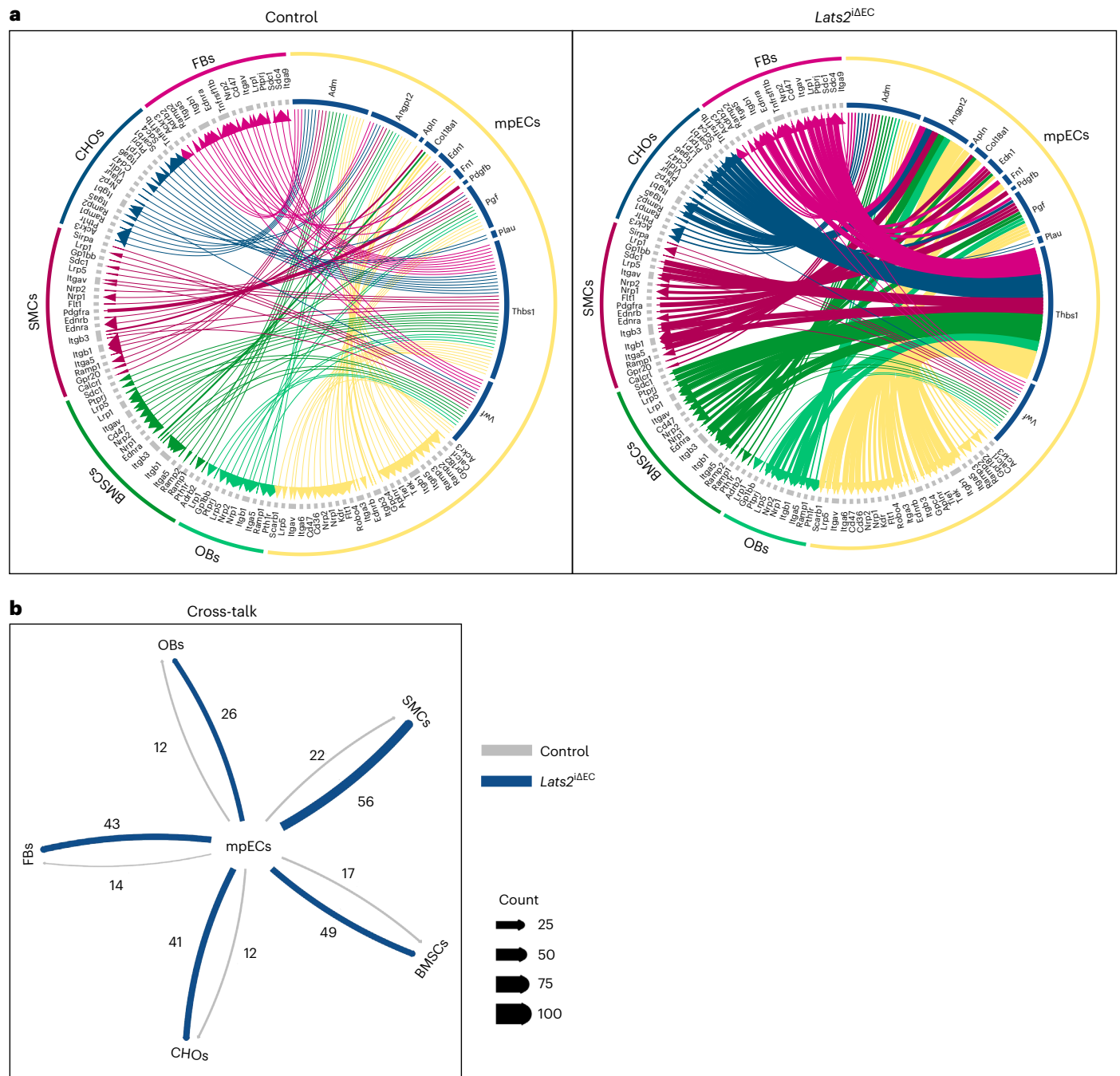


Fig. 8 | Loss of *Lats2* increases endothelial signaling interactions. a, Ligand-receptor pairings indicating increased mpECs signaling to stromal cells in *Lats2*^{ΔEC} mutants. Relative (min-max normalized) changes in normalized expression counts of ligand and receptor for selected interactions (LRI)

(scaled between 0 and 1) originating from mpECs. Interactions are significant at *P*.adj of LRI score in at least one condition and LRIDiffScore ≤ 0.05 and LRIDiff ≥ 1. **b**, Number of significant LRIs between cell types of interest (*P*.adj. LRIScore ≤ 0.05; *P*.adj. LRIDiffScore ≤ 0.05; |LRIDiffScore| ≥ 1). FB, fibroblast.

Discussion

Our results demonstrate that loss of the LATS2 kinase endows bone ECs with disease-promoting properties, resulting in osteosclerotic defects, bone fibrosis, EMH and splenomegaly. This involves the upregulation of YAP1/TAZ, and, accordingly, EC-specific overexpression of stabilized YAP1^{S112A} protein phenocopies major aspects of the defects seen in *Lats2*^{ΔEC} loss-of-function bone. YAP1 and TAZ are well known for their prominent role in the regulation of cell proliferation and tissue growth. In the endothelium of most organs, combined inactivation of *Yap1* and *Taz* impairs angiogenic blood vessel growth^{31,32}, whereas the opposite

phenotype, namely vascular overgrowth, occurs in the postnatal bone vasculature²¹. Our findings presented here indicate that YAP1 and TAZ are no longer required in the adult bone vasculature, and, instead, it is critical for healthy homeostasis that the activity of the two transcriptional coregulators is actively suppressed by LATS2.

Remarkably, loss of LATS2 is not sufficient to cause defects in the endothelium of multiple other organs, which might reflect redundant activity of the related kinase LATS1. It has been shown that LATS1 and LATS2 act non-redundantly in some biological contexts but can often compensate for each other^{33,34}. In ECs of the growing retina and brain,

combined inactivation of *Lats1* and *Lats2* results in hyperproliferation and metabolic activation through upregulation of the proto-oncogene c-Myc, which is rescued by the simultaneous inactivation of *Yap1/Taz*³¹. In the bone endothelium, however, LATS1 is unlikely to be a major player because it cannot prevent major defects in *Lats2*^{ΔEC} mutants.

At the mechanistic level, our results link LATS2 to EndMT, SRF and the regulation of exocytosis. EndMT is a physiological process during embryonic heart development where it mediates the conversion of ECs into valve interstitial cells but also into cardiac pericytes and vascular SMCs³⁵. By contrast, EndMT in the adult organism refers typically to the pathogenic acquisition of a mesenchymal gene signature by ECs in atherosclerosis, hypertension and some other cardiovascular diseases³⁶. SRF is a critical regulator of actin polymerization, which, together with myocardin family cofactors, controls the expression of effectors of actin dynamics and, thereby, myofibroblast differentiation and tissue fibrosis in multiple organs^{37,38}. Cooperation between YAP1/TAZ and SRF was reported for the differentiation of vascular SMCs but also in certain cancer cells and cancer-associated fibroblasts^{39–41}. However, it was also shown that the crosstalk between MRTF-SRF and YAP1/TAZ is often indirect and mediated by cytoskeletal dynamics and cell shape changes^{40,42}. Although the exact nature of the link between SRF and Hippo pathway components in the bone endothelium requires further investigation, our findings show that SRF is required for YAP1/TAZ-induced EndMT, which involves marked changes in EC morphology, gene expression and vascular architecture. These alterations in ECs, through increased expression of matrix molecules and other secreted factors, affect other cell types, most likely mesenchymal mpMSCs/Osteo-CAR cells, resulting in fibrosis and osteosclerotic lesions. Furthermore, the identification of vascular defects in the ThPO and MPL models of myelofibrosis raises the possibility that EndMT, increased biological activity of YAP1/TAZ and SRF-mediated changes in gene expression, but also EC cytoskeletal function, might contribute to fibrosis. These findings are consistent with an earlier study reporting EndMT in ECs of small vessels in the BM and spleen of the JAK2-V617F knock-in mouse model but also in patients with primary myelofibrosis¹⁴. Although the molecular interactions linking diseased hematopoietic cells and blood vessels remain to be unraveled, TGFβ family transforming growth factors were shown to be upregulated in megakaryocytes but also in monocytes/macrophages from patients with myelofibrosis. Inhibition of TGFβ signaling ameliorates fibrosis in vitro and in mouse models of myelofibrosis^{43,44}. TGFβ signaling is also a potent inducer of EndMT, has been linked to the loss (rarefaction) of microvessels and can potentiate MRTF-SRF signaling^{38,45,46}. Future studies will have to address the role of TGFβ and other molecular regulators and provide further insight into the role of blood vessels in animal models of myelofibrosis and in human patients.

Methods

Animal models

For the inducible and EC-specific inactivation of *Lats2* in mice, we bred *Lats2*^{lox/lox} conditional mutants to *Cdh5(PAC)-CreERT2* transgenic mice²¹ to generate Cre-positive EC-specific *Lats2*^{ΔEC} mutants. *Cdh5(PAC)-mT/nG* transgenic reporter mice²¹ were introduced into the *Lats2*^{ΔEC} mutant background and corresponding controls. Mice carrying *loxP*-flanked *Yap1* and *Taz* (*Wwtr1*) alleles⁴⁷ were also bred to the *Cdh5(PAC)-CreERT2* line to generate EC-specific *Yap1*^{lox/lox} and/or *Taz*^{lox/lox} conditional mutants²¹. To generate EC-specific constitutive-active Yap1 knock-in (Yap1-KI), mutated Yap1 amino acid 112 serine to alanine (Yap1^{S112A}) mice²¹ were bred with *Cdh5(PAC)-CreERT2*. Using *Srf*^{lox/lox} mice with a similar breeding strategy, we generated inducible and EC-specific *Srf*^{ΔEC} mutant⁴⁸ and *Lats2 Srf* double loss-of-function mutants (*Lats2 Srf*^{ΔEC}). In all these experiments, Cre-negative littermates subjected to the same tamoxifen administration regime were used as controls. For inducible Cre-mediated recombination, mice received daily intraperitoneal

injections of 1 mg of tamoxifen for 5 d at the age of 4–5 weeks. For the characterization of BMSCs in the metaphysis, *Gli1-CreERT2* (ref. 49) transgenic mice were interbred with Gt(Rosa26) ACTB-tdTomato-EGFP reporter mice⁵⁰. These mice received 1 mg of tamoxifen for 3 d at 8 weeks of age and were analyzed 4 weeks later. Tamoxifen stocks were prepared as described previously²¹. Mice were backcrossed and maintained in a C57/BL6 genetic background, and both sexes were used for analysis.

For the ThPO model of bone fibrosis, wild-type (WT) cKit⁺-enriched cells were transduced with ThPO or empty vector (EV) control lentivirus and transplanted into lethally irradiated (split-dose) B6.Cg-Tg(Ly6a-EGFP)G5Dzk/J (*n* = 5 animals per group) and B6.SJL recipient mice (*n* = 3–4 mice per group). Blood was periodically collected via submandibular bleeds into microtainer tubes (Becton Dickinson), and blood counts were performed on a Horiba Scil Vet abc Plus hematology system. Transplantation of MPL^{WS15L}-expressing and matching control hematopoietic cells into sub-lethally irradiated mice was conducted as described previously⁵¹. Mice were euthanized for analysis when they displayed signs of fibrosis, as indicated by the dropping of hemoglobin levels or weight loss according to defined humane endpoints. Femurs were collected for imaging.

All animal experiments were performed according to institutional guidelines and laws, approved by local animal ethical committees and conducted at the Max Planck Institute for Molecular Biomedicine with necessary permissions (02.04.2015.A185, 84-02.04.2016.A160, 81-02.04.2017.A238 and 81-02.04.2019.A164) granted by the Landesamt für Natur, Umwelt und Verbraucherschutz of North Rhine-Westphalia, Germany. ThPO and MPL bone fibrosis experiments were conducted according to protocols approved by the Central Animal Committee (Centrale Commissie Dierproeven (CCD), The Netherlands) in accordance with legislation in The Netherlands (approval no. AVD1010020173387).

Sample processing and immunostaining

Mice were euthanized, and long bones (femur and tibia) were harvested and fixed immediately in ice-cold 2% paraformaldehyde (PFA) for 6–8 h under gentle agitation. Bones were decalcified in 0.5 MEDTA for 48–72 h at 4 °C under gentle shaking agitation, which was followed by overnight incubation in cryopreservation solution (20% sucrose, 2% PVP) and embedding in bone embedding medium (8% gelatine, 20% sucrose, 2% PVP). Samples were stored overnight at –80 °C. Then, 80–100-μm-thick cryosections were prepared for immunofluorescence staining.

Bone immunostaining was performed as described previously. Bone sections were washed in ice-cold PBS and permeabilized with ice-cold 0.3% Triton X-100 in PBS for 10 min at room temperature (RT). Samples were incubated in blocking solution (5% heat-inactivated donkey serum in 0.3% Triton X-100) for 30 min at RT. Primary antibodies: rat monoclonal anti-endomucin (V.7C7) (Santa Cruz Biotechnology, sc-65495, 1:100 dilution), goat polyclonal anti-CD31 (R&D Systems, AF3628, 1:100 dilution), rabbit polyclonal anti-Fabp5 (Lifespan Biosciences, C312991, 1:100 dilution), goat anti-PDGFRβ (R&D Systems, AF1042, 1:100 dilution), mouse monoclonal alpha-smooth muscle actin-Cy3 (Sigma-Aldrich, C6198, 1:200 dilution), mouse monoclonal alpha-smooth muscle actin-eFluor660 (eBioscience, 50-9760-82, 1:200 dilution), rabbit monoclonal anti-Yap1/Taz (D24E4, Cell Signaling Technology, 8418, 1:100 dilution), rabbit monoclonal anti-vimentin (D21H3, Cell Signaling Technology, 5741, 1:100 dilution), rabbit polyclonal anti-Tagln (Sm22a, Abcam, ab14106, 1:100 dilution), rabbit polyclonal anti-fibronectin (Fn1, Sigma-Aldrich, F3648, 1:100 dilution), rabbit polyclonal anti-thrombospondin 1 (Thbs1, Abcam, ab85762, 1:100 dilution), rabbit polyclonal anti-Angpt2 (Abcam, ab8452, 1:100 dilution), rabbit polyclonal anti-Cav1 (Cell Signaling Technology, 3238, 1:100 dilution), rabbit polyclonal anti-Col4 (AbD Serotec, 2150-1470, 1:100 dilution), rabbit polyclonal anti-Osterix (Abcam, ab22552,

1:300 dilution), goat polyclonal anti-Mmp9 (R&D Systems, AF909, 1:200 dilution), rabbit polyclonal anti-Col-I (Millipore, AB765P, 1:100 dilution), rabbit polyclonal anti-Col-X (Abcam, ab58632, 1:100 dilution), rabbit polyclonal anti-LATS2 (GeneTex, GTX87529, 1:50 dilution), rabbit polyclonal anti-Aggregan (Millipore, AB1031, 1:100 dilution), rabbit anti-vATPaseB1/B2 (Abcam, 200839, 1:100 dilution), rat anti-mouse Ter119 (BD Biosciences, 553673, 1:200 dilution), rat anti-mouse B220 (BD Biosciences, 553090, 1:200 dilution), rat-monoclonal anti-active Itgb1 (BD Biosciences, 553715, 1:500 dilution), rabbit polyclonal anti-FAK (pY397) (Thermo Fisher Scientific, 44-624G, 1:50 dilution), rabbit monoclonal anti-Runx2 (Abcam, ab192256, 1:200 dilution) or rat monoclonal anti-Srf (from Alfred Nordheim, 1:50 dilution) were diluted in 5% donkey serum mixed PBS and incubated overnight at 4 °C. Next, slides were washed 3–5 times in PBS in 5–10-min intervals. Species-specific Alexa Fluor secondary antibodies Alexa Fluor 488 (Thermo Fisher Scientific, A21208), Alexa Fluor 546 (Thermo Fisher Scientific, A11056), Alexa Fluor 594 (Thermo Fisher Scientific, A21209), Alexa Fluor 647 (Thermo Fisher Scientific, A31573 or A21447) or Phalloidin-488 (Invitrogen, A12379) diluted 1:100 in PBS were added and incubated for 2–3 h at RT. Immunostained bone sections were imaged with a Leica SP8 confocal microscope.

Vascular permeability assay

To conduct in vivo vascular permeability tests on adult mice, 100 μ l of 1 mg of Dextran Texas Red (Thermo Fisher Scientific, D1830, 70,000 MW) was injected into the tail vein and left to circulate for 15 min. Femurs were removed from euthanized mice, immediately dropped in ice-cold 4% PFA and fixed overnight. Fluorescence microscopy was used to capture images of the femur without any signal enhancement.

Histological staining methods

For Safranin O staining, long bones from *Lats2*^{ΔEC} mutants and control animals were harvested, fixed and decalcified. The bones were dehydrated and embedded using paraffin wax by stranded histology methods. Bone paraffin blocks were cut at 5 μ m, and sections were deparaffinized and hydrated. Then, stain with 0.1% Safranin O for 8 min and wash with water. Next, slides were dehydrated and dried and mounted with non-aqueous mounting medium (Entellan, Sigma-Aldrich).

AZAN trichrome staining after deparaffinization and hydration of the slides. After 5 min at 55 °C in the azocarmin solution, the slides were washed with distilled water. The sections were then immersed in an aniline-ethanol solution for 18 minutes, before they were exposed to 1% acetic acid in ethanol solution for 45 s. Next, rinse with distilled water and then immerse in 5% phosphotungstic acid for 2 h. After that, place in a mixture of Aniline Blue–Orange G for 8 min. Use distilled water to rinse. Next, sections were dehydrated and mounted.

For Reticulin staining, bones were hydrated with distilled water. After a 5-min addition of potassium permanganate solution, distilled water was used to rinse. The next solutions—oxalic acid, silver nitrate, gold chloride and sodium thiosulfate—were added for 2 min and then individually washed with distilled water. Sections were dehydrated and mounted.

Calcein Green and Alizarin Red double labeling assay

For in vivo double labeling with Calcein Green and Alizarin Red, 10-week-old control and *Lats2*^{ΔEC} mutant mice were injected intraperitoneally with 100 μ l of Calcein Green (40 mg kg⁻¹; Sigma-Aldrich, C0875) and 100 μ l of Alizarin Red (40 mg kg⁻¹; Sigma-Aldrich, A3882) 1 week later. Mice were euthanized at 12 weeks, and femurs were dissected and immediately placed in ice-cold 4% PFA for overnight fixation. Next, samples were cryopreserved, embedded in bone embedding media and kept at –80 °C overnight. Bones were cryosectioned

at 30- μ m thickness, stained for 30 min with DAPI and then washed twice with washing buffer before imaging by confocal fluorescence microscopy.

μ CT analysis

Femurs were fixed in 4% PFA overnight at 4 °C and subjected to μ CT analysis by Scanco Medical AG. In the whole three-dimensional evaluation of the trabecular structure, distal section of femur, a voxel size of 5 μ m was used. We evaluated 833 slices covering 4.988 mm in height for each sample.

Fluorescence-activated cell sorting

Single-cell suspensions were prepared from bone and spleen as described above. Primary antibody lineage cell detection cocktail-biotin (Miltenyi Biotec, 130-092-613), rat monoclonal anti-Ly6A-PE-cy7 (BD Pharmingen, clone D7, 558162), rat monoclonal anti-CD117-APC (BD Pharmingen, clone 2B8, 553356), hamster monoclonal anti-CD3e-FITC (eBioscience, clone 145-2C11, 11-0031), rat monoclonal anti-B220-APC (Invitrogen, RA3-6B2, RM2605), rat monoclonal anti-CD11b-APC (BioLegend, M1/70, 101212), rat monoclonal anti-Ly-6G(Gr-1)-BV605 (BioLegend, RB6-8C5, 108440), rat monoclonal anti-CD45-PE (BD Pharmingen, 30-F11, 553081), rat monoclonal anti-TER-119-APC (eBioscience, 17-5921) or rat monoclonal anti-CD41-BV605 (BioLegend, MWReg30, 133921) were diluted in fluorescence-activated cell sorting (FACS) buffer (2% FCS, 0.5% BSA in PBS solution) and incubated with cells on ice for 40 min. Cells were washed 2–3 times in FACS buffer and incubated with secondary antibodies for 40 min. Cells were washed two further times and used for flow cytometry. Cells were resuspended in FACS buffer supplemented with 1 mg ml⁻¹ DAPI to allow exclusion of non-viable cells when required. Cell sorting was performed on a FACSAriaIIu cell sorter (BD Biosciences). Cell analysis was performed using FlowJo software.

BMSC in vitro culture and quantitative PCR

BMSCs were isolated from metaphysis of WT mice and cultured as described previously⁵². For agonist-induced BMSC differentiation assay, cells were serum starved for overnight and then stimulated with agonist TGF- β 1, Endothelin-1 (ET-1) or Adrenomedullin (ADM) for 24 h and analyzed for quantitative PCR. Next, total RNA was isolated from these cells using an RNA Plus Mini Kit (Qiagen, 74134) according to the manufacturer's instructions. RNA was reverse transcribed using the an iScript cDNA Synthesis Kit (Bio-Rad, 1708890). Quantitative PCR was carried out using gene-specific TaqMan probes Eukaryotic *18S rRNA* (4319413E), *Acta2* (Mm00725412_s1), *Tagln* (Mm00441661_g1) and *Fn1* (Mm01256744_m1) (Thermo Fisher Scientific) using a C1000 Touch thermal cycler (Bio-Rad).

Electron microscopy

Femurs were removed and directly cut into half in fixative. For ultrastructural analysis, fixative comprised 2% glutaraldehyde, 2% PFA, 20 mM CaCl₂, 20 mM MgCl₂ in 0.1 M cacodylate buffer, pH 7.4. Fixed material was post-fixed in 1% osmium tetroxide containing 1.5% potassium ferrocyanide, dehydrated, including uranyl-en-bloc staining, and embedded stepwise in epon. Ultramicrotomy was performed until reaching the area of interest, where 60-nm ultra-thin sections were collected on formvar-coated 1 slot copper grids. Sections were further stained with lead citrate and finally analyzed with a transmission electron microscope (Tecnai-12-biotwin, Thermo Fisher Scientific).

Bone stromal cells preparation for scRNA-seq

For scRNA-seq analysis, femur and tibia were harvested from *Lats2*^{ΔEC} mutant and control mice and cleaned from attached surrounding tissue before the metaphysis region was dissected and collected in digestion enzyme solution (Collagenase type I and type IV, 2 mg ml⁻¹). Next, bones were crushed using mortar and pestle. Samples were digested for 45 min at 37 °C under gentle agitation. Digested samples were

transferred to 70- μ m strainers in 50-ml tubes to obtain a single-cell suspension, which was resuspended in blocking solution (1% BSA, 1 mM EDTA in PBS without $\text{Ca}^{2+}/\text{Mg}^{2+}$), centrifuged at 300g for 5 min, washed 2–3 times with ice-cold blocking solution and filtered through 50- μ m strainers. Pellets were resuspended in respective volume of blocking solution. Single-cell suspensions were subjected to lineage depletion using a lineage cell depletion kit (MACS, 130-090-858) following the manufacturer's instructions. Next, lineage-negative (Lin^-) cells were depleted by CD45 and CD117 using microbeads (MACS, 130-052-301 and 130-091-224) from Lin^- bone cells to enrich bone stromal cells. The remaining cells were resuspended to final concentration of 10^6 cells per milliliter in 0.05% BSA in PBS, examined by microscopy and used for scRNA-seq.

Single-cell suspensions were subjected to droplet-based scRNA-seq. Single cells were encapsulated into emulsion droplets using the Chromium controller (10x Genomics). scRNA-seq libraries were prepared using a Chromium Single Cell 3' Reagent Kit (V3) (10x Genomics, PN-10000075) according to the manufacturer's protocol. scRNA-seq libraries were evaluated and quantified by an Agilent Bioanalyzer using a High Sensitivity DNA Kit (cat. no. 5067-4626) and a Qubit (Thermo Fisher Scientific, Q32851). Individual libraries were diluted to 4 nM and pooled for sequencing. Pooled libraries were sequenced by using a High Output Kit (150 cycles) (Illumina, TG-160-2002) with a NextSeq 500 sequencer (Illumina).

scRNA-seq data analysis

Detailed settings for the analysis steps mentioned below can be found in the accompanying GitLab repository (see 'Data availability' section) and in Supplementary Table 1. Default parameters were used, if not detailed otherwise, there or in the text below.

Read data quality control and mapping. Illumina sequencing results were demultiplexed and converted to FASTQ format using Illumina bcl2fastq software (version 2.20.0.422). Raw reads were processed using cutadapt⁵³ (version 3.5). Pre-processed read data were aligned to the mouse reference genome (version GRCh39) with GENCODE M26 annotation⁵⁴ extended by adding sequences for CreERT2 and Rosa26-mTmG and counted with STARsolo⁵⁵ (version 2.7.10a) using its electron microscopy implementation and GeneFull_Ex50pAS read counting. The official 10x Genomics barcode whitelist⁵⁶ was used.

Data filtering and visualization. Pre-processing of the feature-count-matrix output by STARsolo was largely performed within the Python (version 3.8.10)-based scanpy (version 1.9.1) ecosystem⁵⁷. Exceptions are functionalities that are only available for R (ref. 58) (version 4.2.1). These include: sequencing depth normalization using scan (version 1.24.1)⁵⁹, doublet detection using scDblFinder (version 1.11.4)⁶⁰ and calculation of DEGs using DESeq2 (version 1.36)⁶¹. All visualization was done using matplotlib (version 3.5.3)⁶² functions. Barcodes with fewer than 1,000 unique molecular identifiers (UMIs) or fewer than 800 features (>0 counts per feature) detected were discarded. Similarly, only barcodes with less than 15% of counts stemming from mitotic genes or 5% from hemoglobin genes were retained. Furthermore, barcodes were filtered for a complexity value above 0.8, where complexity is defined as the \log_{10} -transformed number of expressed genes divided by the \log_{10} -transformed number of total counts per barcode. Additionally, only genes with at least 10 counts total from at least 10 distinct barcodes were kept. scanpy normalization was applied using `min.size = 100` and `min.mean = 0.1` in the `quickCluster` and `computeSumFactors` functions, respectively. The separate samples were merged into one `AnnData` (version 0.8.0) object; 4,000 highly variable genes were calculated from the normalized matrix; and the matrix was scaled to unit variance and zero mean, capping values at 10. The 50 first principal components were used for integration using Harmony-Py⁶³ (version 0.0.9, Python implementation by Kamil Slowikowski) with

`max_iter_harmony = 1,000`, `max_iter_kmeans = 1,000`, `epsilon_cluster = 1×10^{-6}` and `epsilon_harmony = 1×10^{-5}` . Uniform manifold approximation and projection (UMAP) dimensionality reduction⁶⁴ and Leiden clustering⁶⁵ at a resolution of 1 were performed. The resulting 30 clusters, the uncorrected principal component analysis (PCA) embedding and the raw count and normalized matrices were used for scDblFinder doublet prediction. Barcode clusters were annotated with the broad cell identity that they most likely represent based on marker genes provided in Supplementary Table 1. Undesired populations, such as myeloid or lymphoid cells; clusters of barcodes that, either manually based on gene expression or by scDblFinder, could be classified as consisting of more than 20% doublets; and very small clusters (<100 cells) were removed. All remaining 20,383 barcodes will hereafter be referred to as cells.

For each of the four main groups of broad cell identities defined previously, we created subsets and performed scaling, PCA calculation, harmony-py integration, UMAP visualization and Leiden clustering anew as before, to detect more fine-grained sub-cell-type identities. Details on the settings used in each subclustering and marker genes used for annotation can be found in Supplementary Table 1. Some subclustering revealed small cell clusters that could not be identified based on their expression and were, therefore, removed. The subset was then visualized in a second passthrough (indicated in Supplementary Table 1) with the same settings as the first one. Afterwards, either all subsets (20,184 cells) or only the mp-MSK and SMC subsets were merged again for comprehensive visualization and analysis.

Pseudotime analysis was performed using slingshot⁶⁶ (version 2.6.0). We defined the mpMSC cluster as starting and the Myh11 SMC cluster as the end node of the trajectory. Cells were binned into 21 bins of equal cell numbers along the pseudotime trajectory. Gene-to-gene Pearson correlation of normalized and z-scaled gene expression counts across the ordered pseudotime bins was calculated for the top 8,000 highly variable genes. Correlations with a correlation coefficient above 0.5 were kept, and the data were transformed into an igraph (Python igraph 0.10.4)⁶⁷ network with genes representing nodes and their mutual correlation coefficients representing the edge weights. Leiden clustering was applied with a resolution parameter of 1.

Differential gene expression (DGE) analysis was performed using DESeq2 on pseudobulk expression matrices. When the expression of genes in one cluster was to be compared to several other clusters, all pairwise comparisons were calculated, and then the mean \log_2 fold change (FC) of these comparisons was output as \log_2 FC, and the minimum *P* value ($\alpha = 0.01$) calculated from the respective adjusted *P* values using `scipy.stats.combine_pvalues` function (version 1.9.1)⁶⁸ was used as 'adjusted *P* value' of the upregulation of gene expression in the cluster of interest. It was also counted in how many comparisons the overexpression in the cell cluster of interest compared to each other one was above a \log_2 FC threshold of 2. If not mentioned otherwise, only genes expressed in at least 20% of cells of the respective group in either condition were kept.

Radial expression plots were created by calculating DGE (using DESeq2) between the control and conditional knockout (cKO) conditions for each cell identity presented in the respective graph. Only genes expressed in at least 20% of cells of the respective group in either condition were kept. Each quadrant represents genes with upregulated expression in the respective condition and cell type. For each quadrant, all \log_2 FC values below 0 were set to 0, and the accompanying adjusted *P* values were set to 1. Then, genes were plotted in a scatterplot by jittering points on the *x* axis, representing their \log_2 FC on the *y* axis and the adjusted *P* value of the expression difference as the point color. This means that, per cell population, all genes present in the analysis are represented in each quadrant, showing which of these are upregulated in the respective condition and cell type. The main goal of this plot is to show in which condition and cell types most genes are differentially expressed.

Additional computational analyses. Differential abundance of cell neighborhoods was quantified using milopy (version 0.1.0)⁶⁹ with $\alpha = 0.01$. Potentially regulating transcription factors for selected gene sets were calculated using the iRegulon⁷⁰ plugin to Cytoscape (version 3.9.1)⁷¹ with the 6K Motif collection, looking 500 bp upstream of provided genes in seven species. PAGA²⁸ was applied to the data with default settings via scanpy's implementation.

Predicting LRIs. To determine possible LRIs, a permutation-based approach similar to the one introduced in CellPhoneDB⁷² was used. The normalized count matrix was used as a basis for 10,000 cell type label permutations where cell type labels were randomly re-assigned. Ligand–receptor (LR) gene identity and interaction pairs were taken from the consensus database of LIANA⁷³, excluding bidirectional annotations and genes expressed in less than 10% of cells. For each LR interaction, first the mean expression of the ligand (Lmean) and receptor (Rmean) were calculated for each cell type in each condition, and then an interaction score (LRIScore) was calculated for all possible cell type interactions per condition separately as the product of Lmean and Rmean. This approach differs from the methodology employed by CellPhoneDB in that our approach uses the product instead of the mean value of ligand and receptor mean expression. This is intended to implicitly penalize interactions where one or both partners are lowly expressed. Based on the number of permutation results matching or exceeding the observed value, values of P were calculated for each interaction. Values of P calculated in this test are approximations of P but will be referred to as P values nonetheless. Multiple testing correction was performed using the Benjamini–Hochberg⁷⁴ implementation in the statsmodels (version 0.13.1)⁷⁵ function `multiplerep` on all P values. These corrected P values will be referenced as adjusted P values. Additionally, using the created background distribution, the z-score of the original LRIScore was determined.

In the same fashion as for cell type labels, condition labels (control/cKO) were permuted an equal number of times as cell type labels and a difference score between the LRI scores of the two conditions were calculated for each cell type interaction as:

$$LRIDiff_{score} = \frac{\log 2(Lmean_{cKO}/Lmean_{control}) + \log 2(Rmean_{cKO}/Rmean_{control})}{2}$$

This scoring is similar to a previously proposed perturbation score⁷⁶, but the mean and not the product of the absolute \log_2FC was used. This was done to emphasize coordinated upregulation or downregulation of ligand and receptor instead of just the overall magnitude of change. P values and adjusted P values were calculated from these scores in a manner sensitive to the direction of change and used to assess differences in LRI scores between conditions. This is similar to a very recently published approach⁷⁷.

This procedure was done once for a dataset, where, of all ECs, only mpECs were kept, and major cell type labels were used for all other cells. Another analysis focused on mpECs, mpMSCs, bmMSCs, Myh11⁺ and Myh11⁻ SMCs compared to all other major cell types as background, but only the results for the mentioned subtypes were visualized.

Statistics and reproducibility

Images were analyzed, quantified and processed using Volocity (PerkinElmer), Fiji (ImageJ) and Adobe Photoshop and Illustrator software 2020.

Statistical analysis was performed using GraphPad Prism 9 software or the R statistical environment (<http://r-project.org>). All data are presented as mean values \pm s.e.m. unless indicated otherwise. Comparisons between two groups were performed with unpaired two-tailed Mann–Whitney test. Comparisons between more than two groups were made by Tukey multiple comparison test to determine statistical significance. $P < 0.05$ was considered significant unless

stated otherwise. For DGE (Figs. 5d and 6a,b and Extended Data Fig. 7g): DESeq2 (internally uses Wald test statistics) yielding false discovery rate (FDR)-corrected P values (P_{adj}). Extended Data Fig. 9a: genes filtered based on pairwise comparisons between mp-ECs and all other EC subtypes using DESeq2 yielding FDR-corrected P values (P_{adj}) combined across comparisons using the Fisher method implemented in `scipy's combine_p_values` function. LR pairings and the significant interactions between cell types of interest (Fig. 6g,h) were analyzed with a permutation test (one-sided) with Benjamini–Hochberg-corrected P values (P_{adj}). Extended Data Fig. 9a,c,d used a permutation test (one-sided) with Benjamini–Hochberg-corrected P values (P_{adj}). Four biological independent samples were used in Figs. 1e,f, 2i,j and 5f, and three biological independent samples were used in Figs. 3a,e and 4c and Extended Data Figs. 1c–e, 2b–g, 3b, 4f–h, 5f,g,i, 6a and 8b–d. Sample numbers are indicated in the figure legends and were chosen based on experience from previous experiments. Reproducibility was ensured by more than three independent experiments (aside from scRNA-seq). No statistical method was used to predetermine sample size, and no animals were excluded from analysis.

Reporting summary

Further information on research design is available in the Nature Portfolio Reporting Summary linked to this article.

Data availability

The scRNA-seq data generated in this study have been deposited in the Gene Expression Omnibus under accession number [GSE225429](https://www.ncbi.nlm.nih.gov/geo/query/acc.cgi?acc=GSE225429). The mouse reference genome GRCm39 with GENCODE M26 annotation (https://www.gencodegenes.org/mouse/release_M26.html) was used for mapping the reads in this study. All other relevant data supporting the key findings of this study are available within the article and its Supplementary Information files.

Code availability

All code used to produce the computational analysis results and figures in this publication are available at https://gitlab.gwdg.de/pmajev/sivaraj_majev_lats2_ecs. The assigned DOI is <https://doi.org/10.5281/zenodo.11456485>.

References

- Zahr, A. A. et al. Bone marrow fibrosis in myelofibrosis: pathogenesis, prognosis and targeted strategies. *Haematologica* **101**, 660–671 (2016).
- Li, B. et al. Bone marrow fibrosis grade is an independent risk factor for overall survival in patients with primary myelofibrosis. *Blood Cancer J.* **6**, e505 (2016).
- Boudin, E. & Van Hul, W. Sclerosing bone dysplasias. *Best Pract. Res. Clin. Endocrinol. Metab.* **32**, 707–723 (2018).
- Spampinato, M. et al. Focus on osteosclerotic progression in primary myelofibrosis. *Biomolecules* **11**, 122 (2021).
- Mizoguchi, T. et al. Osterix marks distinct waves of primitive and definitive stromal progenitors during bone marrow development. *Dev. Cell* **29**, 340–349 (2014).
- Zhou, B. O., Yue, R., Murphy, M. M., Peyser, J. G. & Morrison, S. J. Leptin-receptor-expressing mesenchymal stromal cells represent the main source of bone formed by adult bone marrow. *Cell Stem Cell* **15**, 154–168 (2014).
- Shi, Y. et al. Gli1 identifies osteogenic progenitors for bone formation and fracture repair. *Nat. Commun.* **8**, 2043 (2017).
- Kramann, R. et al. Perivascular Gli1⁺ progenitors are key contributors to injury-induced organ fibrosis. *Cell Stem Cell* **16**, 51–66 (2015).
- Decker, M. et al. Leptin-receptor-expressing bone marrow stromal cells are myofibroblasts in primary myelofibrosis. *Nat. Cell Biol.* **19**, 677–688 (2017).

10. Schneider, R. K. et al. Gli1⁺ mesenchymal stromal cells are a key driver of bone marrow fibrosis and an important cellular therapeutic target. *Cell Stem Cell* **20**, 785–800 (2017).
11. Leimkuhler, N. B. et al. Heterogeneous bone-marrow stromal progenitors drive myelofibrosis via a druggable alarmin axis. *Cell Stem Cell* **28**, 637–652 (2021).
12. Psaila, B. et al. Single-cell analyses reveal megakaryocyte-biased hematopoiesis in myelofibrosis and identify mutant clone-specific targets. *Mol. Cell* **78**, 477–492 (2020).
13. Vannucchi, A. M. et al. A pathobiologic pathway linking thrombopoietin, GATA-1, and TGF- β 1 in the development of myelofibrosis. *Blood* **105**, 3493–3501 (2005).
14. Erba, B. G. et al. Endothelial-to-mesenchymal transition in bone marrow and spleen of primary myelofibrosis. *Am. J. Pathol.* **187**, 1879–1892 (2017).
15. Ding, L., Saunders, T. L., Enikolopov, G. & Morrison, S. J. Endothelial and perivascular cells maintain haematopoietic stem cells. *Nature* **481**, 457–462 (2012).
16. Kusumbe, A. P., Ramasamy, S. K. & Adams, R. H. Coupling of angiogenesis and osteogenesis by a specific vessel subtype in bone. *Nature* **507**, 323–328 (2014).
17. Kretschmer, M., Rudiger, D. & Zahler, S. Mechanical aspects of angiogenesis. *Cancers* **13**, 4987 (2021).
18. Moya, I. M. & Halder, G. Hippo-YAP/TAZ signalling in organ regeneration and regenerative medicine. *Nat. Rev. Mol. Cell Biol.* **20**, 211–226 (2019).
19. Yu, F. X. & Guan, K. L. The Hippo pathway: regulators and regulations. *Genes Dev.* **27**, 355–371 (2013).
20. Piccolo, S., Dupont, S. & Cordenonsi, M. The biology of YAP/TAZ: Hippo signaling and beyond. *Physiol. Rev.* **94**, 1287–1312 (2014).
21. Sivaraj, K. K. et al. YAP1 and TAZ negatively control bone angiogenesis by limiting hypoxia-inducible factor signaling in endothelial cells. *eLife* **9**, e50770 (2020).
22. Bando, Y. et al. Expression of epidermal fatty acid binding protein (E-FABP) in septoclasts in the growth plate cartilage of mice. *J. Mol. Histol.* **45**, 507–518 (2014).
23. Sivaraj, K. K. et al. Mesenchymal stromal cell-derived septoclasts resorb cartilage during developmental ossification and fracture healing. *Nat. Commun.* **13**, 571 (2022).
24. Levine, R. L., Pardanani, A., Tefferi, A. & Gilliland, D. G. Role of JAK2 in the pathogenesis and therapy of myeloproliferative disorders. *Nat. Rev. Cancer* **7**, 673–683 (2007).
25. Yan, X. Q. et al. A model of myelofibrosis and osteosclerosis in mice induced by overexpressing thrombopoietin (mpl ligand): reversal of disease by bone marrow transplantation. *Blood* **88**, 402–409 (1996).
26. Pikman, Y. et al. *MPLW515L* is a novel somatic activating mutation in myelofibrosis with myeloid metaplasia. *PLoS Med.* **3**, e270 (2006).
27. Haghverdi, L., Buttner, M., Wolf, F. A., Buettner, F. & Theis, F. J. Diffusion pseudotime robustly reconstructs lineage branching. *Nat. Methods* **13**, 845–848 (2016).
28. Wolf, F. A. et al. PAGA: graph abstraction reconciles clustering with trajectory inference through a topology preserving map of single cells. *Genome Biol.* **20**, 59 (2019).
29. Efremova, M., Vento-Tormo, M., Teichmann, S. A. & Vento-Tormo, R. CellPhoneDB: inferring cell–cell communication from combined expression of multi-subunit ligand–receptor complexes. *Nat. Protocols* **15**, 1484–1506 (2020).
30. Janky, R. et al. iRegulon: from a gene list to a gene regulatory network using large motif and track collections. *PLoS Comput. Biol.* **10**, e1003731 (2014).
31. Kim, J. et al. YAP/TAZ regulates sprouting angiogenesis and vascular barrier maturation. *J. Clin. Invest.* **127**, 3441–3461 (2017).
32. Wang, X. et al. YAP/TAZ orchestrate VEGF signaling during developmental angiogenesis. *Dev. Cell* **42**, 462–478 (2017).
33. McPherson, J. P. et al. Lats2/Kpm is required for embryonic development, proliferation control and genomic integrity. *EMBO J.* **23**, 3677–3688 (2004).
34. Furth, N. & Aylon, Y. The LATS1 and LATS2 tumor suppressors: beyond the Hippo pathway. *Cell Death Differ.* **24**, 1488–1501 (2017).
35. Chen, Q. et al. Endothelial cells are progenitors of cardiac pericytes and vascular smooth muscle cells. *Nat. Commun.* **7**, 12422 (2016).
36. Kovacic, J. C. et al. Endothelial to mesenchymal transition in cardiovascular disease: JACC State-of-the-Art Review. *J. Am. Coll. Cardiol.* **73**, 190–209 (2019).
37. Olson, E. N. & Nordheim, A. Linking actin dynamics and gene transcription to drive cellular motile functions. *Nat. Rev. Mol. Cell Biol.* **11**, 353–365 (2010).
38. Small, E. M. The actin–MRTF–SRF gene regulatory axis and myofibroblast differentiation. *J. Cardiovasc. Transl. Res.* **5**, 794–804 (2012).
39. Liu, C. Y. et al. MRTF/SRF dependent transcriptional regulation of TAZ in breast cancer cells. *Oncotarget* **7**, 13706–13716 (2016).
40. Foster, C. T., Gualdrini, F. & Treisman, R. Mutual dependence of the MRTF–SRF and YAP–TEAD pathways in cancer-associated fibroblasts is indirect and mediated by cytoskeletal dynamics. *Genes Dev.* **31**, 2361–2375 (2017).
41. Pagiatakis, C., Sun, D., Tobin, S. W., Miyake, T. & McDermott, J. C. TGF β -TAZ/SRF signalling regulates vascular smooth muscle cell differentiation. *FEBS J.* **284**, 1644–1656 (2017).
42. Fearing, B. V. et al. Mechanosensitive transcriptional coactivators MRTF-A and YAP/TAZ regulate nucleus pulposus cell phenotype through cell shape. *FASEB J.* **33**, 14022–14035 (2019).
43. Varricchio, L. et al. TGF- β 1 protein trap AVID200 beneficially affects hematopoiesis and bone marrow fibrosis in myelofibrosis. *JCI Insight* **6**, e145651 (2021).
44. Lecomte, S. et al. Therapeutic activity of GARP:TGF- β 1 blockade in murine primary myelofibrosis. *Blood* **141**, 490–502 (2023).
45. Qiu, P., Feng, X. H. & Li, L. Interaction of Smad3 and SRF-associated complex mediates TGF- β 1 signals to regulate *SM22* transcription during myofibroblast differentiation. *J. Mol. Cell. Cardiol.* **35**, 1407–1420 (2003).
46. Goumans, M. J., van Zonneveld, A. J. & ten Dijke, P. Transforming growth factor β -induced endothelial-to-mesenchymal transition: a switch to cardiac fibrosis? *Trends Cardiovasc. Med.* **18**, 293–298 (2008).
47. Reginensi, A. et al. Yap- and Cdc42-dependent nephrogenesis and morphogenesis during mouse kidney development. *PLoS Genet.* **9**, e1003380 (2013).
48. Wiebel, F. F., Rennekampff, V., Vintersten, K. & Nordheim, A. Generation of mice carrying conditional knockout alleles for the transcription factor SRF. *Genesis* **32**, 124–126 (2002).
49. Ahn, S. & Joyner, A. L. Dynamic changes in the response of cells to positive Hedgehog signaling during mouse limb patterning. *Cell* **118**, 505–516 (2004).
50. Muzumdar, M. D., Tasic, B., Miyamichi, K., Li, L. & Luo, L. A global double-fluorescent Cre reporter mouse. *Genesis* **45**, 593–605 (2007).
51. Gleitz, H. F. E. et al. Increased CXCL4 expression in hematopoietic cells links inflammation and progression of bone marrow fibrosis in MPN. *Blood* **136**, 2051–2064 (2020).
52. Sivaraj, K. K. et al. Regional specialization and fate specification of bone stromal cells in skeletal development. *Cell Rep.* **36**, 109352 (2021).

53. Martin, M. Cutadapt removes adapter sequences from high-throughput sequencing reads. *EMBnet.journal* **17**, 10–12 (2011).
54. Frankish, A. et al. GENCODE reference annotation for the human and mouse genomes. *Nucleic Acids. Res.* **47**, D766–D773 (2019).
55. Dobin, A. et al. STAR: ultrafast universal RNA-seq aligner. *Bioinformatics* **29**, 15–21 (2013).
56. Zheng, G. X. Y. et al. Massively parallel digital transcriptional profiling of single cells. *Nat. Commun.* **8**, 14049 (2017).
57. Wolf, F. A., Angerer, P. & Theis, F. J. SCANPY: large-scale single-cell gene expression data analysis. *Genome Biol.* **19**, 15 (2018).
58. R Core Team. R: a language and environment for statistical computing. <https://www.R-project.org/> (2017).
59. Lun, A. T. L., Bach, K. & Marioni, J. C. Pooling across cells to normalize single-cell RNA sequencing data with many zero counts. *Genome Biol.* **17**, 75 (2016).
60. Germain, P.-L., Lun, A., Meixide, C. G., Macnair, W. & Robinson, M. D. Doublet identification in single-cell sequencing data using *scDblFinder*. *F1000Res.* **10**, 979 (2022).
61. Love, M. I., Huber, W. & Anders, S. Moderated estimation of fold change and dispersion for RNA-seq data with DESeq2. *Genome Biol.* **15**, 550 (2014).
62. Hunter, J. D. Matplotlib: a 2D graphics environment. *Comput. Sci. Eng.* **9**, 90–95 (2007).
63. Korsunsky, I. et al. Fast, sensitive and accurate integration of single-cell data with Harmony. *Nat. Methods* **16**, 1289–1296 (2019).
64. McInnes, L., Healy, J., Saul, N. & Großberger, L. UMAP: uniform manifold approximation and projection. *J. Open Source Softw.* **3**, 861 (2018).
65. Traag, V. A., Waltman, L. & van Eck, N. J. From Louvain to Leiden: guaranteeing well-connected communities. *Sci. Rep.* **9**, 5233 (2019).
66. Street, K. et al. Slingshot: cell lineage and pseudotime inference for single-cell transcriptomics. *BMC Genomics* **19**, 477 (2018).
67. Csárdi, G. & Nepusz, T. The Igraph software package for complex network research. *InterJournal Complex Systems*, 1695 (2006).
68. Virtanen, P. et al. SciPy 1.0: fundamental algorithms for scientific computing in Python. *Nat. Methods* **17**, 261–272 (2020).
69. Dann, E., Henderson, N. C., Teichmann, S. A., Morgan, M. D. & Marioni, J. C. Differential abundance testing on single-cell data using *k*-nearest neighbor graphs. *Nat. Biotechnol.* **40**, 245–253 (2022).
70. Janky, R. S. et al. iRegulon: from a gene list to a gene regulatory network using large motif and track collections. *PLoS Comput. Biol.* **10**, e1003731 (2014).
71. Shannon, P. et al. Cytoscape: a software environment for integrated models of biomolecular interaction networks. *Genome Res.* **13**, 2498–2504 (2003).
72. Vento-Tormo, R. et al. Single-cell reconstruction of the early maternal–fetal interface in humans. *Nature* **563**, 347–353 (2018).
73. Dimitrov, D. et al. Comparison of methods and resources for cell–cell communication inference from single-cell RNA-Seq data. *Nat. Commun.* **13**, 3224 (2022).
74. Benjamini, Y. & Hochberg, Y. Controlling the false discovery rate: a practical and powerful approach to multiple testing. *J. R. Stat. Soc. Series B Methodol.* **57**, 289–300 (1995).
75. Seabold, S. & Perktold, J. Statsmodels: econometric and statistical modeling with Python. In *Proc. of the 9th Python in Science Conference*. 92–96 (SciPy, 2010).
76. Raredon, M. S. B. et al. Single-cell connectomic analysis of adult mammalian lungs. *Sci. Adv.* **5**, eaaw3851 (2019).
77. Lagger, C. et al. scDiffCom: a tool for differential analysis of cell–cell interactions provides a mouse atlas of aging changes in intercellular communication. *Nat. Aging* **3**, 1446–1461 (2023).

Acknowledgements

We thank K. Kruse for providing feedback on the computational methods used in this work as well as for support and fruitful scientific discussions. We thank K. Mildner for helping with electron microscopy sample preparation. This work was supported by the Max Planck Society (R.H.A.), the Deutsche Forschungsgemeinschaft (CRC 1366; RHA), the Leducq Foundation (R.H.A.) and the European Research Council (AdG 786672, PROVEC; AdG 101139772, PROTECT) (R.H.A.).

Author contributions

K.K.S., P.-G.M. and R.H.A. designed experiments and interpreted results. K.K.S. generated and characterized mouse mutant lines and conducted all experiments, including FACS, bone sectioning and staining, confocal imaging, quantifications and scRNA-seq. P.-G.M. and K.K.S. analyzed the scRNA-seq data. B.D. performed staining and analysis. M.S. performed FACS. D.Z. performed electron microscopy. S.S. provided technical assistance. A.N. generated and contributed reagents and mouse strains. B.B. and R.K.S. performed the ThPO fibrosis experiment. K.K.S., P.-G.M. and R.H.A. wrote the manuscript.

Funding

Open access funding provided by Max Planck Society.

Competing interests

R.K.S. is a co-founder and shareholder of Sequantrix GmbH and a consultant for Active Biotech. The other authors declare no competing interests.

Additional information

Extended data is available for this paper at <https://doi.org/10.1038/s44161-024-00508-x>.

Supplementary information The online version contains supplementary material available at <https://doi.org/10.1038/s44161-024-00508-x>.

Correspondence and requests for materials should be addressed to Kishor K. Sivaraj, Rebekka K. Schneider or Ralf H. Adams.

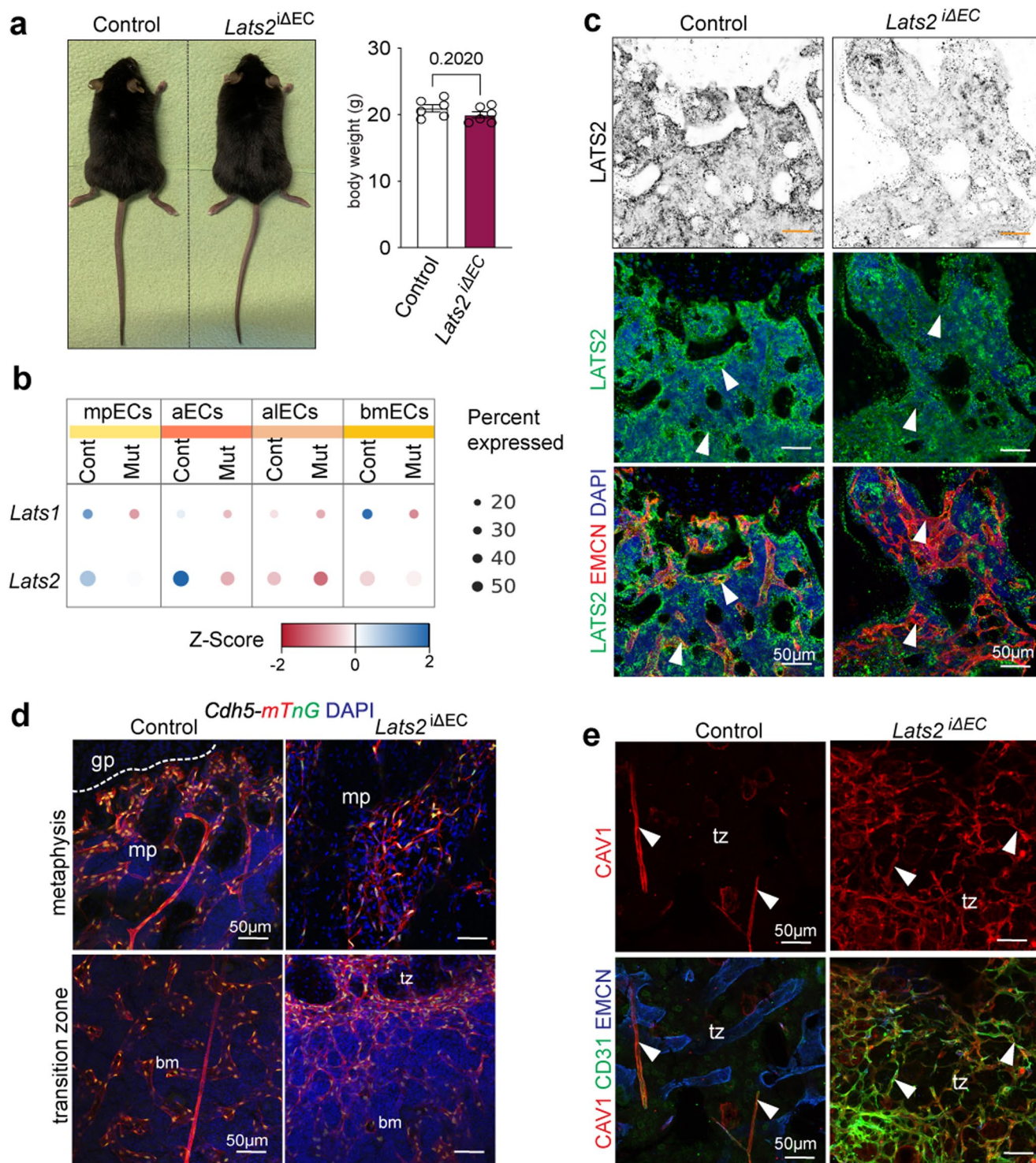
Peer review information *Nature Cardiovascular Research* thanks Mei Xin and the other, anonymous, reviewer(s) for their contribution to the peer review of this work.

Reprints and permissions information is available at www.nature.com/reprints.

Publisher's note Springer Nature remains neutral with regard to jurisdictional claims in published maps and institutional affiliations.

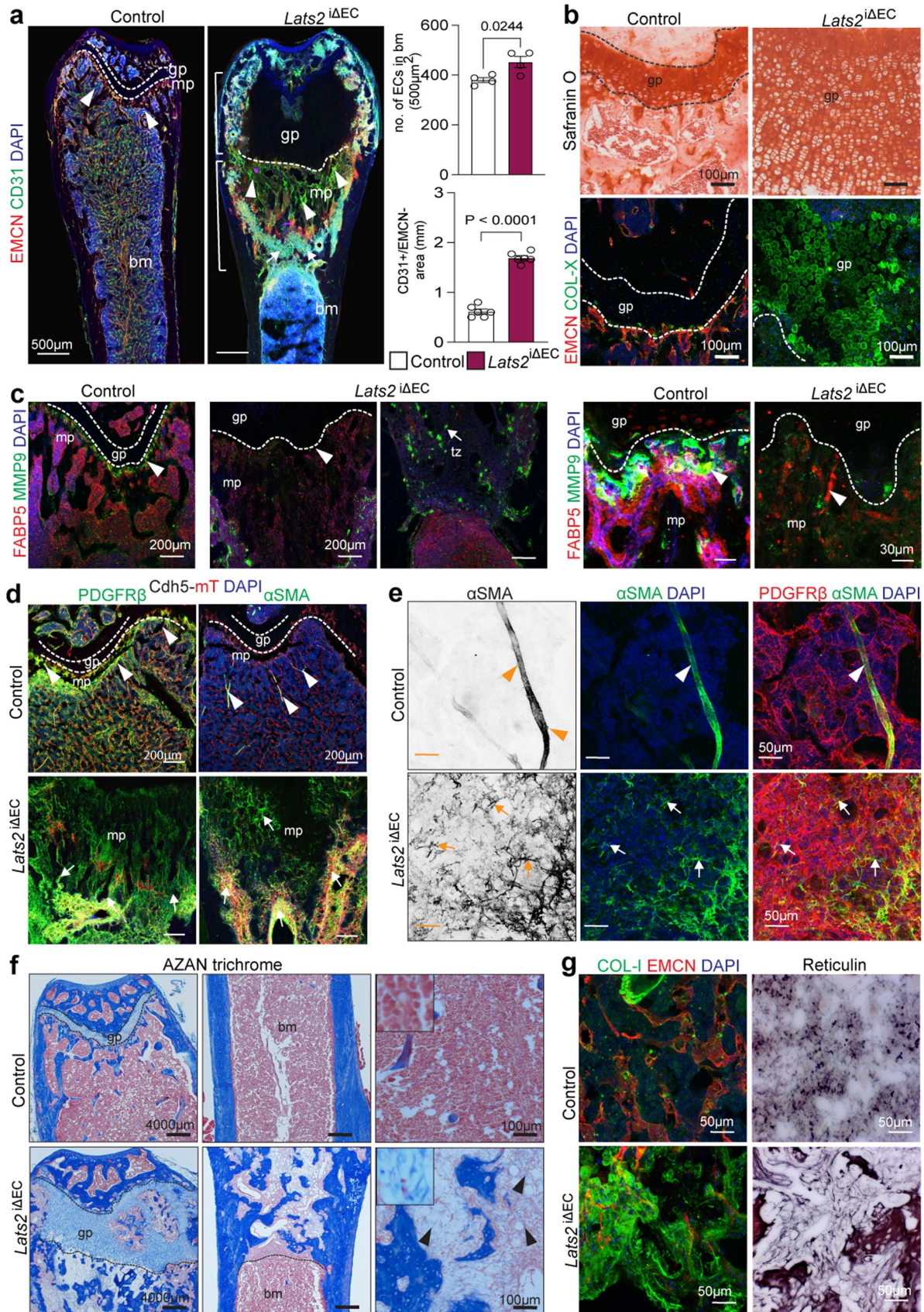
Open Access This article is licensed under a Creative Commons Attribution 4.0 International License, which permits use, sharing, adaptation, distribution and reproduction in any medium or format, as long as you give appropriate credit to the original author(s) and the source, provide a link to the Creative Commons licence, and indicate if changes were made. The images or other third party material in this article are included in the article's Creative Commons licence, unless indicated otherwise in a credit line to the material. If material is not included in the article's Creative Commons licence and your intended use is not permitted by statutory regulation or exceeds the permitted use, you will need to obtain permission directly from the copyright holder. To view a copy of this licence, visit <http://creativecommons.org/licenses/by/4.0/>.

© The Author(s) 2024



Extended Data Fig. 1 | Loss of endothelial *Lats2* induces vascular defects in bone. **a.** *Lats2*^{iΔEC} mutant mice look normal and body weight is comparable to control littermates ($n = 6$). Data shown as mean \pm SEM. P values, Mann–Whitney test (two-tailed). **b.** Dot plot for normalised and averaged expression indicates of *Lats1* and *Lats2* expression in the indicated control (Cont) and *Lats2*^{iΔEC} mutant (Mut) EC subpopulations. Z-scaled per row. Note reduction of *Lats2* transcripts and absence of compensatory *Lats1* upregulation. **c.** Reduced LATS2 immunostaining (gray/green) in *Lats2*^{iΔEC} mutant bone endothelium (EMCN, red)

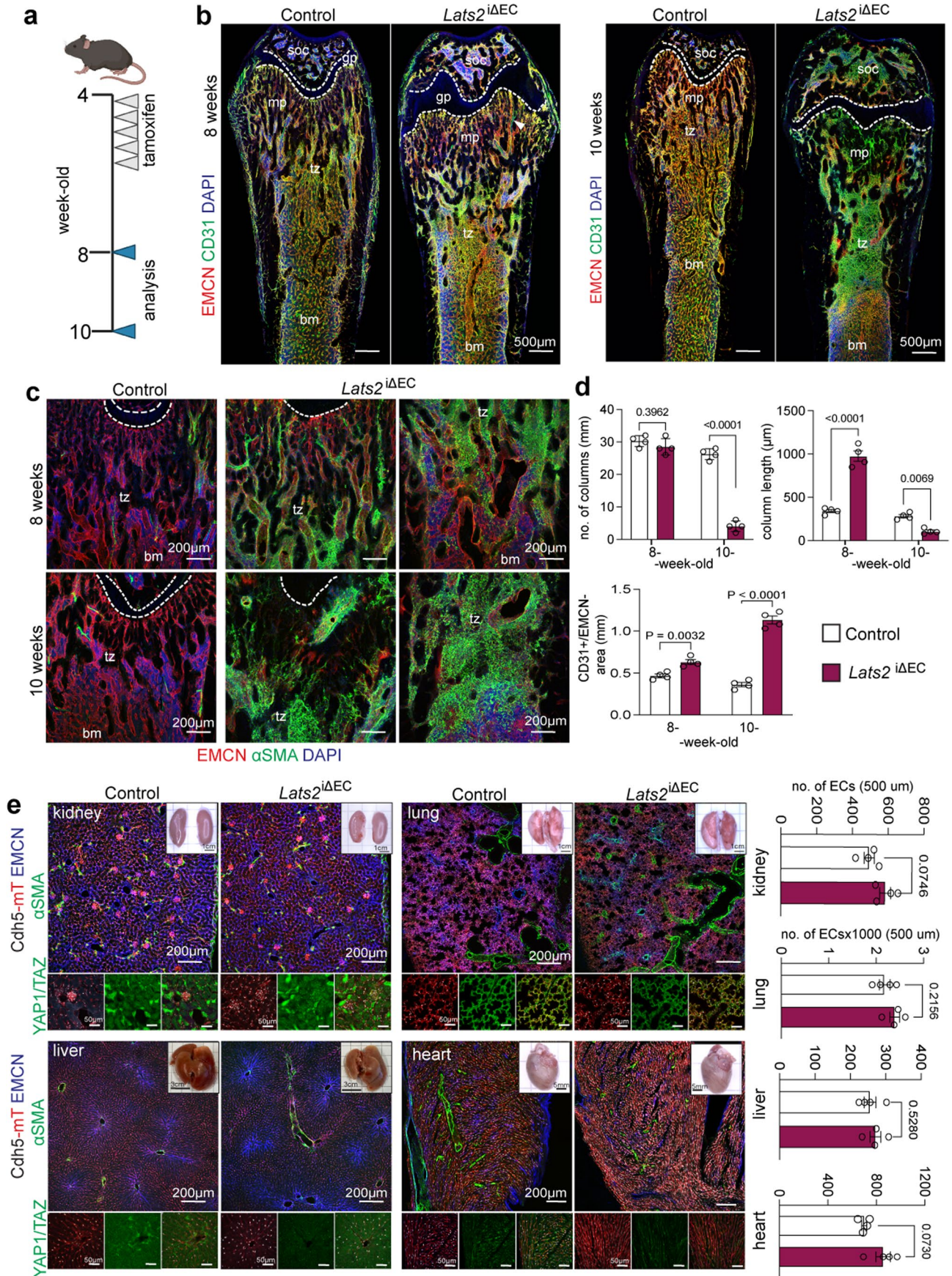
(arrowheads). Nuclei, DAPI (blue). **d.** Representative high magnification images of control and *Lats2*^{iΔEC} mutant in *Cdh5-mTnG* reporter background. Femoral metaphysis (mp), bone marrow (bm), growth plate (gp) and transition zone between metaphysis and diaphysis (tz) are indicated. **e.** Representative confocal images showing increase CAV1+ (red), CD31+ (green) and EMCN+ (red) ECs in *Lats2*^{iΔEC} femoral transition zone (tz). Note that CAV1 labels artery in control but microvascular structures in mutant (arrowheads). $n =$ independent biological samples.



Extended Data Fig. 2 | See next page for caption.

Extended Data Fig. 2 | Bone defects after loss of *Lats2* in ECs. **a.** Tile scan confocal longitudinal views of EMCN and CD31 stained femoral blood vessels. Note enlargement of *Lats2*^{ΔEC} growth plate and metaphysis. Type H capillaries are visible in control but are replaced by CD31+/EMCN- ECs in mutants (arrowheads). Graphs on the right show quantification of ECs in bone marrow (bm) (top) and CD31+/EMCN- capillaries (bottom) (n = 6). Data presented as mean ± SEM. P values, Mann–Whitney test (two-tailed). **b.** Representative images showing expansion of hypertrophic chondrocytes in *Lats2*^{ΔEC} mutants by Safranin O staining and collagen type X (COL-X) immunostaining. **c.** FABP5+ septoclasts and MMP9 expression (arrowheads) at chondro-osseous border near growth

plate (gp) are lost in *Lats2*^{ΔEC} mutants. **d, e.** *Lats2*^{ΔEC} femurs show increase in PDGFRβ+ and αSMA+ immunosignals (arrows). αSMA+ in control is largely confined to arterial SMCs (arrowheads) (**d**). Higher magnification images are shown in (**e**). **f.** AZAN trichrome staining of femoral sections showing expansion of the *Lats2*^{ΔEC} growth plate (gp) (left) and ectopic bone (center). Insets on the right show deposition of collagen fibers (arrowheads), which is visible at high magnification. **g.** Representative images showing increased collagen type I (COL-I) immunosignal and reticulin stained fibers in *Lats2*^{ΔEC} mutant sections. n = independent biological samples.

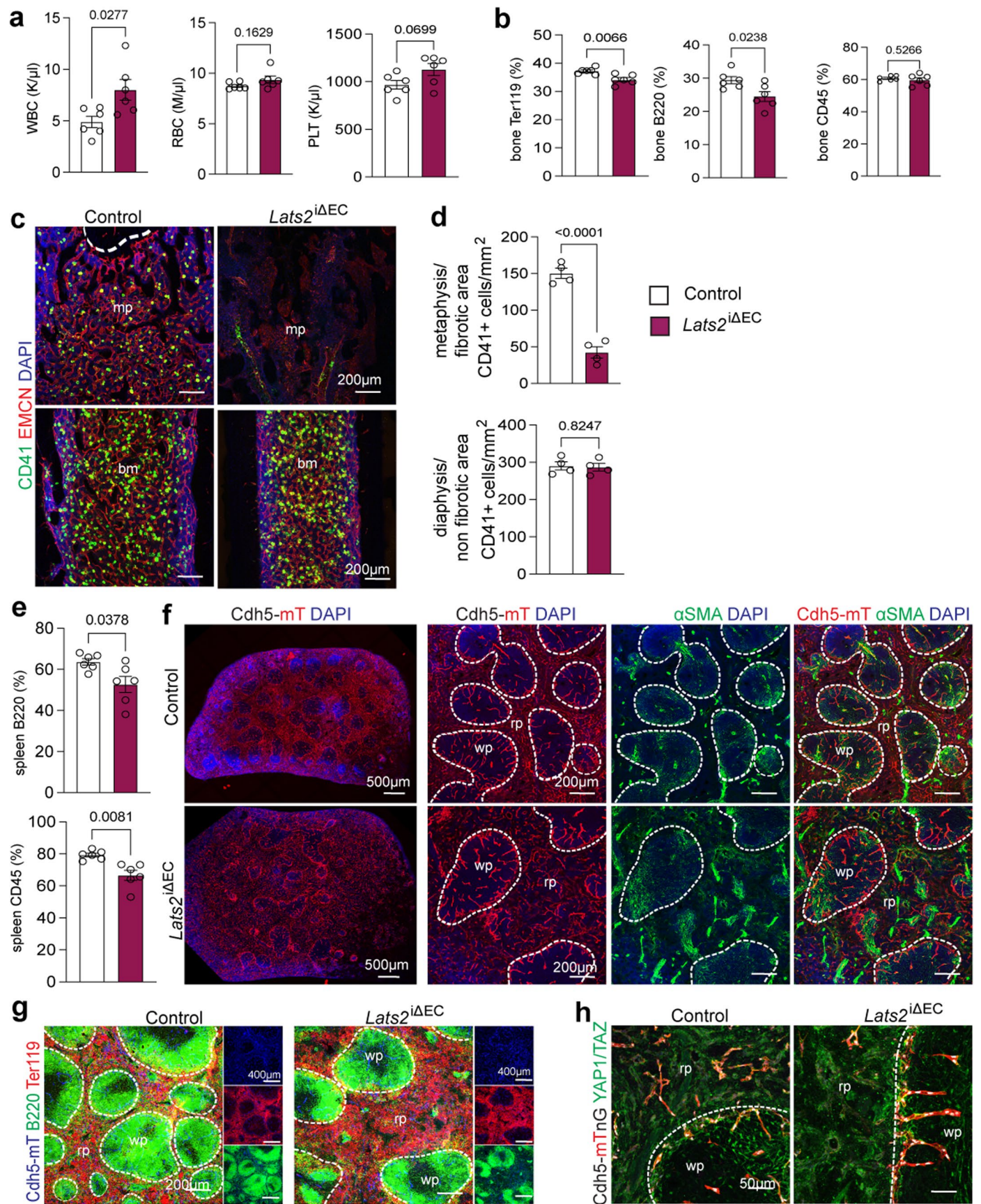


Extended Data Fig. 3 | See next page for caption.

Extended Data Fig. 3 | Loss of *Lats2* in ECs promotes bone fibrosis.

a, b. Tamoxifen injection scheme (**a**). Tile scan confocal longitudinal view of femurs stained for EMCN (red) and CD31 (green) in 8 and 10-week-old control or *Lats2*^{ΔEC} mutant mice (**b**). Nuclei, DAPI (blue). **c.** Confocal images of αSMA+ (green) cells in 8-week-old and 10-week-old control or *Lats2*^{ΔEC} femoral metaphysis (mp). EMCN (red), DAPI (blue). **d.** Quantification of number and

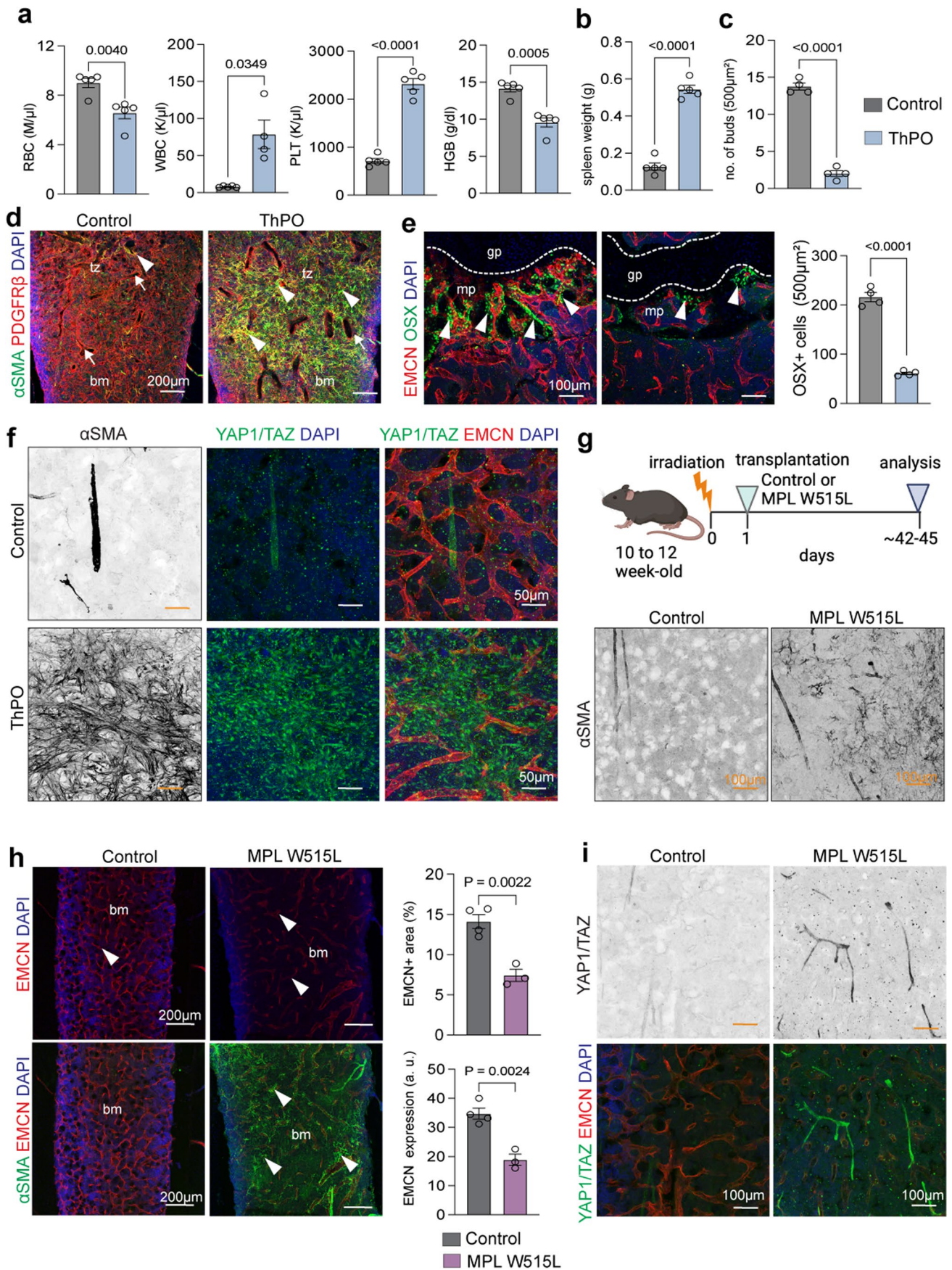
length of vessels columns as well as CD31+/EMCN- area ($n = 4$). Data presented as mean \pm SEM. P values, Mann–Whitney test (two-tailed). **e.** Representative images of control and *Lats2*^{ΔEC} organs in the *Cdh5-mTnG* reporter background. Sections are stained for αSMA, EMCN and YAP1/TAZ, as indicated. Quantification shows that EC number is unchanged in these organs ($n = 4$). Data shown as mean \pm SEM. P values, Mann–Whitney test (two-tailed). $n =$ independent biological samples.



Extended Data Fig. 4 | See next page for caption.

Extended Data Fig. 4 | Blood cells and spleen morphology in *Lats2*^{ΔEC} mutants. a, b. Quantification of white blood cells (WBC), red blood cells (RBC), and platelets (PLT) in peripheral blood (**a**). FACS analysis of Ter119⁺, B220⁺, and CD45⁺ cell frequencies in bone (**b**). **c, d.** Representative confocal images of CD41⁺ megakaryocytes (green) in control and *Lats2*^{ΔEC} femoral sections (**c**). Quantification shows significant reduction of CD41⁺ cells in the *Lats2*^{ΔEC} metaphysis fibrotic area but not in diaphysis of non-fibrotic area (**d**). **e.** Quantification of B220⁺ and CD45⁺ cell frequencies in spleen. **f.** Confocal tile scans of control and *Lats2*^{ΔEC} spleen vasculature labelled with the *Cdh5-mTnG*

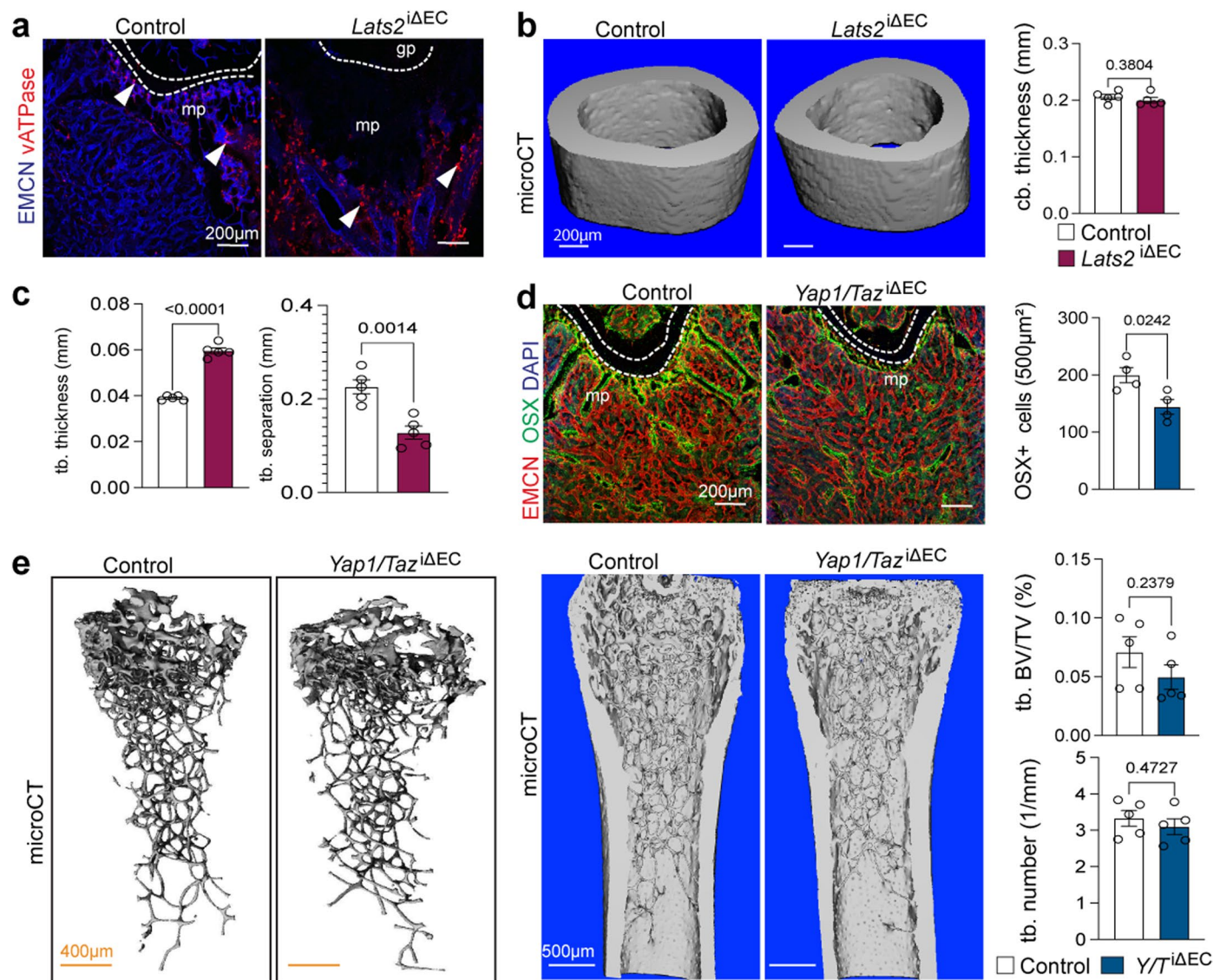
reporter (left). Images at high magnification show αSMA (green), ECs (*Cdh5-mTnG*, red), and DAPI (blue). White pulp (wp) and red pulp (rp) are indicated. **g, h.** Representative confocal images of the spleen showing B220 (green) and Ter119 (red) positive white pulp (wp) and red pulp (rp), respectively. Blood vessels (*Cdh5-mT*, blue) (**g**). Immunostaining of YAP1/TAZ in *Cdh5-mTnG* reporter of control and *Lats2*^{ΔEC} spleen (**h**). Sample number is n = 6 (a, b), n = 4 (d), n = 6 (e). Data are presented as mean ± SEM. P values, Mann-Whitney test (two-tailed). n = independent biological samples.



Extended Data Fig. 5 | See next page for caption.

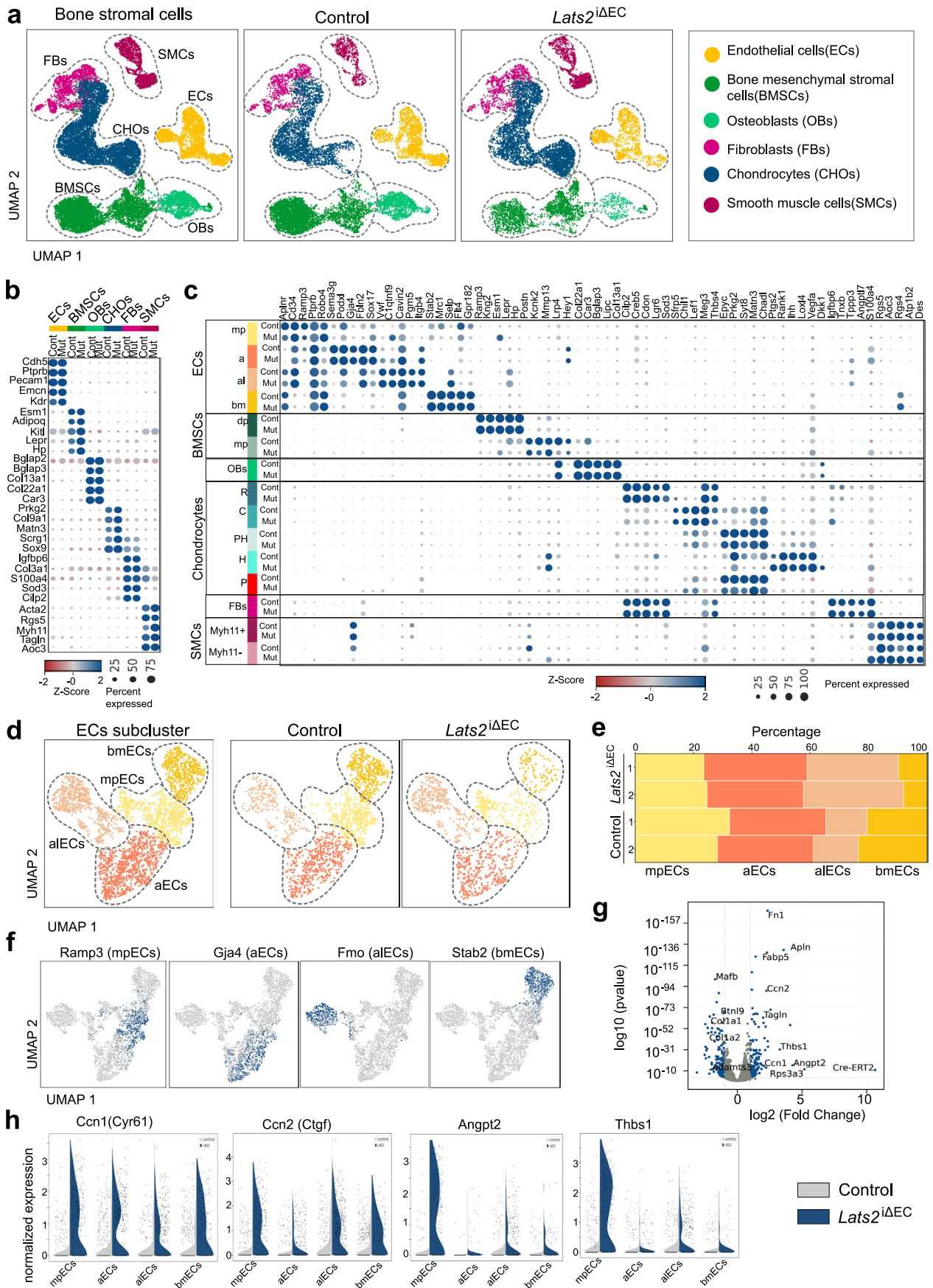
Extended Data Fig. 5 | YAP1/TAZ expression in ThPO- or MPL induced myelofibrosis. a-c. Quantification of white blood cells (WBC), red blood cells (RBC) and platelets (PLT) in peripheral blood (**a**), spleen weight (**b**), and number of type H vessel buds (**c**) in control and ThPO gain-of-function bone. ($n = 5$). Data are presented as mean \pm SEM. P values, Mann-Whitney test (two-tailed). **d, e.** Representative confocal images showing increase of α SMA immunosignals in diaphysis (**d**) and reduction of OSX+ cells (**e**) in ThPO femur relative to control. ($n = 4$). Data are presented as mean \pm SEM. P values, Mann-Whitney test (two-tailed). **f.** Representative confocal images showing strong and widespread increase in α SMA (gray) immunostaining together with increased YAP1/TAZ

expression ThPO-treated BM. **g.** Experimental scheme of MPL^{W515L}-induced BM fibrosis. Representative confocal images (bottom) show α SMA immunostaining in control and MPL^{W515L} (MPL) bone sections. **h.** Confocal images showing reduced EMCN+ (red) vessels and increase of α SMA (green) signal in MPL bone relative to control. Nuclei, DAPI (blue). Graphs on the right show decreased EMCN+ vessels area and expression in MPL bones. ($n = 3-4$). Data shown as mean \pm SEM. P values, Mann-Whitney test (two-tailed). **i.** Immunostaining of YAP1/TAZ (green), EMCN (red), and DAPI (blue) as indicated, in control and MPL bone sections. n = independent biological samples.



Extended Data Fig. 6 | Endothelial Hippo signaling in adult bone. **a.** Confocal images showing vATPase+ osteoclasts (red, arrowheads) in *Lats2*^{ΔEC} femur. **b, c.** Representative microCT images of cortical bone (cb) in *Lats2*^{ΔEC} and control femur (**b**). Graphs show quantitative analysis of trabecular bone (tb) thickness, tb separation, and cortical bone thickness (**c**). **d.** Representative confocal images and quantification showing slight reduction of femoral OSX+ cells in *Yap1/Taz*^{ΔEC}

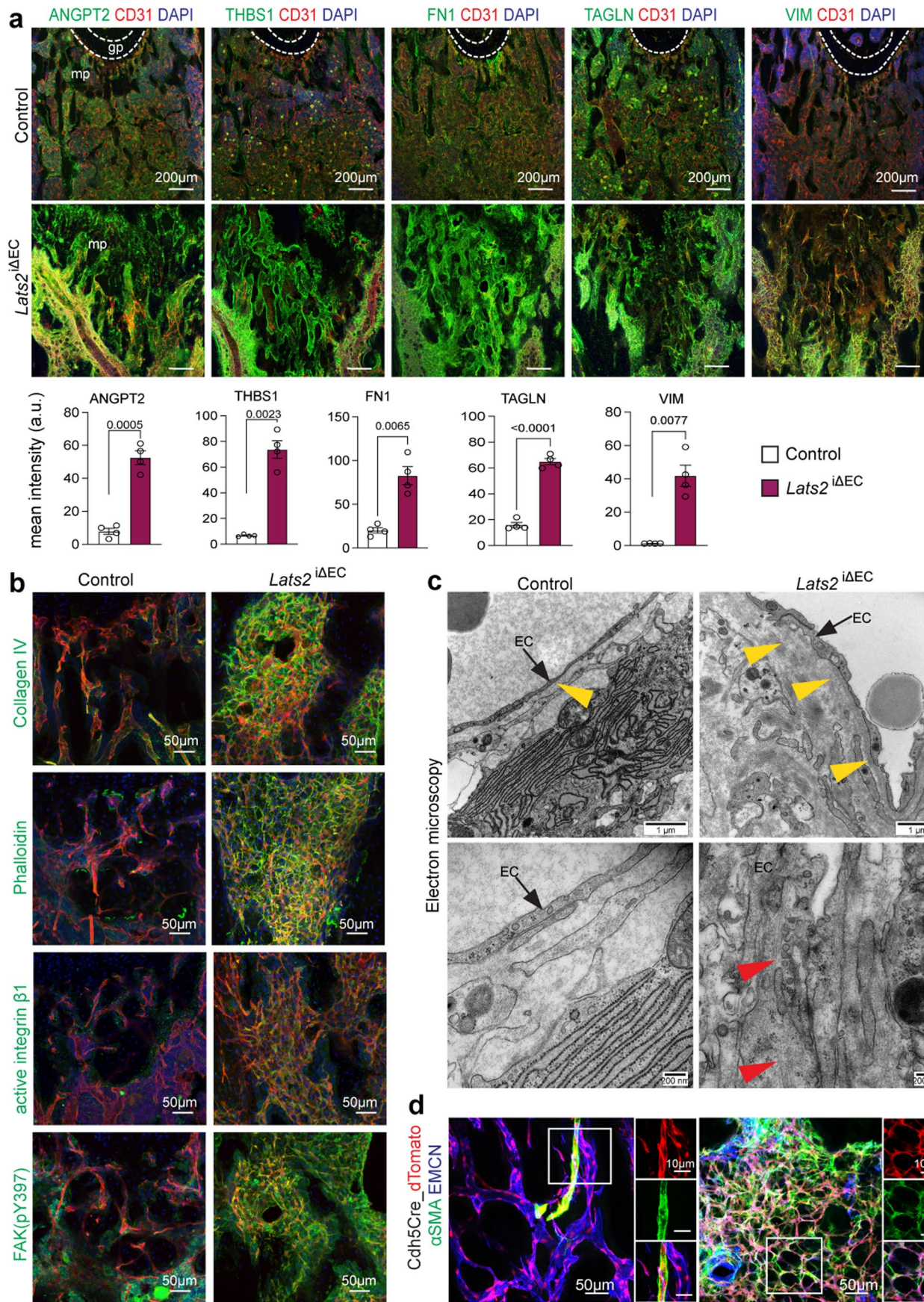
double mutant relative to littermate control. **e.** Representative μCT images of trabecular bone in control and *Yap1/Taz*^{ΔEC} femur. Quantitative analysis of trabecular (tb) volume (BV/TV, bone volume/total volume) and tb number. Sample numbers $n = 5$ (b, c), $n = 4$ (d), $n = 5$ (e). Data are presented as mean \pm SEM. P values, statistical analysis performed using the Mann-Whitney test (two-tailed). n = independent biological samples.



Extended Data Fig. 7 | See next page for caption.

Extended Data Fig. 7 | scRNA-sequencing of non-hematopoietic cells from bone. **a-c.** UMAP plot showing color-coded cell clusters of control and *Lats2*^{ΔEC} bone stromal cells (**a**). Markers for main bone stromal cell populations (**b**) and their subclusters (**c**) are shown in dot plots. **d-f.** UMAP plot of EC subsets, split by condition (right) (**d**). Bar graph displaying percentage of endothelial cells subtypes in control and *Lats2*^{ΔEC} mutants (**e**). UMAP plot colored by normalized expression of EC subset identity marker genes: *Ramp3* (metaphyseal ECs,

mpECs), *Gja4* (arterial ECs, aEC), *Fmo* (arteriole-like ECs, alECs) and *Stab2* (bone marrow ECs, bm) (**f**). **g, h.** Volcano plot of differentially expressed genes (frac. expressed > 0.2 in either condition) between control and mutant condition across all ECs (blue color: log₂FC ≥ 1, p.adj ≤ 0.001.) (**g**). Visualisation of selected known Hippo pathway target genes: *Ccn1* (Cyr61), *Ccn2* (Ctgf), *Angpt2* and *Thbs1* in *Lats2*^{ΔEC} mutant and control (**h**).



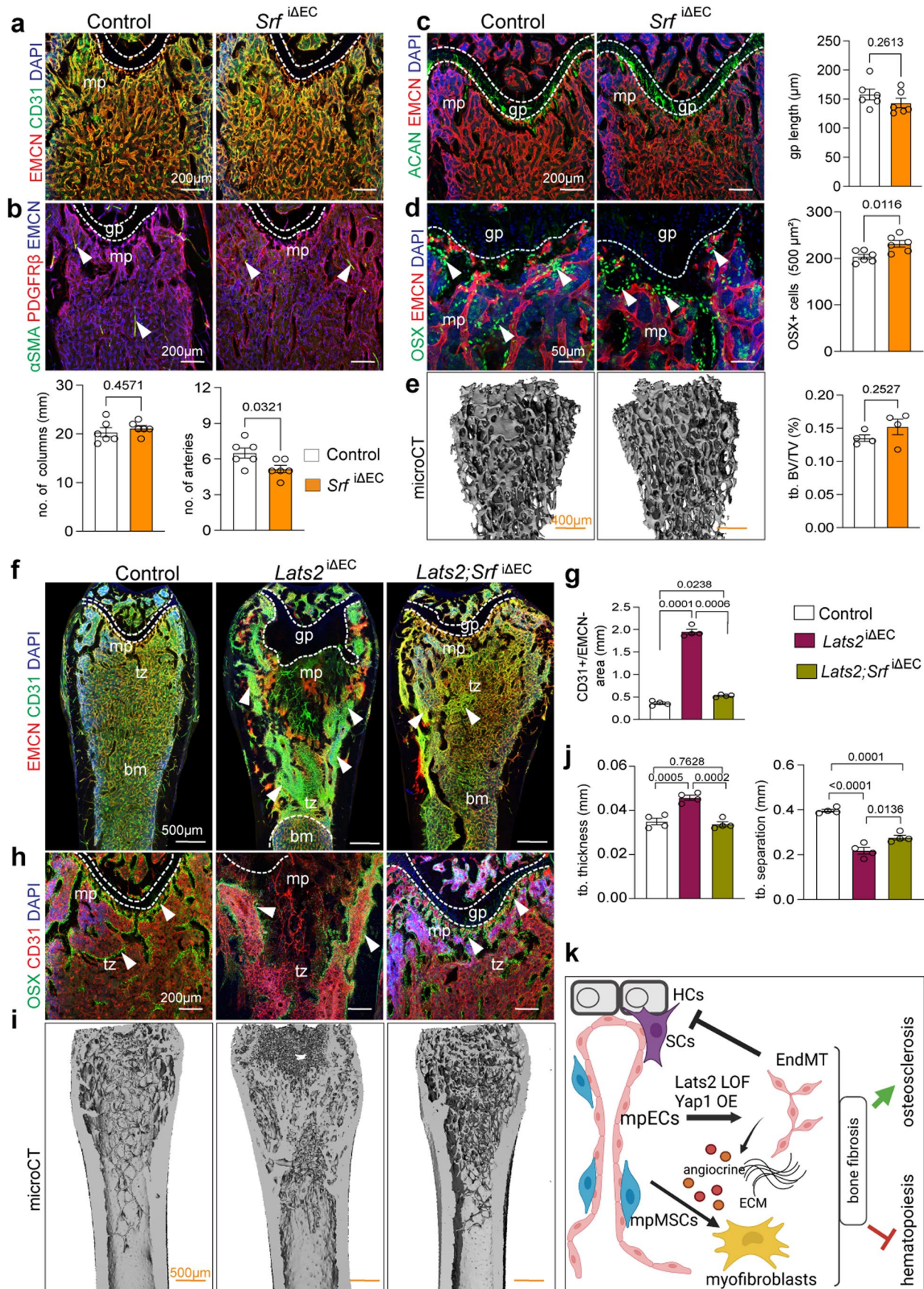
Extended Data Fig. 8 | See next page for caption.

Extended Data Fig. 8 | EndMT in *Lats2*^{ΔEC} bone endothelium. **a.** Confocal images showing strongly elevated Angiopoietin 2 (ANGPT2), Thrombospondin 1 (THBS1), Fibronectin 1 (FNI), Transgelin (TAGLN), and Vimentin (VIM) expression in *Lats2*^{ΔEC} bone sections. ($n = 4$). Data in graphs are presented as mean \pm SEM. P values, statistical analysis performed using the Mann–Whitney test (two-tailed). **b.** Confocal images showing increased staining for collagen IV (COL IV), the actin cytoskeleton (with Phalloidin), active-integrin β 1 and phosphorylated

focal adhesion kinase (FAK pY397) in *Lats2*^{ΔEC} mutant relative to control. **c.** Transmission electron micrographs showing increased subendothelial basement membrane and accumulation of ECM (yellow arrowheads) in *Lats2*^{ΔEC} femur. Mutant ECs are rich in actin filaments (red arrowheads). **d.** Confocal images of *Lats2*^{ΔEC} mutant in *R26-dTomato* reporter background showing α SMA staining in dTomato+ ECs. In control samples, α SMA signal is confined to SMCs covering arteries. $n =$ independent biological samples.

Extended Data Fig. 9 | Angiocrine signals and EC-BMSC cross-talk. a. Ligands showing on average significantly ($\log_2FC \geq 1$, $p_{adj} \leq 0.05$, $frac. \text{expressed} \geq 0.1$) larger counts in mutant mpECs than in any other EC subidentity and are significantly elevated (see Methods) relative to at least one other EC subpopulation. **b.** Selected ligand-receptor pairings of main bone stromal cells, which are increased in *Lats2* ^{Δ EC} mutants. **c.** Mean normalized expression counts of selected, significant ligand-receptor interactions (p_{adj} of LRI score in either condition and LRIDiff Scores ≤ 0.05 , $|LRIDiff| \geq 1$) in mpECS and all other major celltypes. Ligand (left, dark blue bar) and receptor (right, red

bar). **d.** Mean normalized expression counts of selected, significant ligand-receptor interactions (p_{adj} of LRI score in either condition and LRIDiff Scores ≤ 0.05 , $LRIDiff \geq 1$) in mpECS, mpMSCs and SMCs. Ligand (left, dark blue bar) and receptor (right, red bar). **e.** Quantitative PCR (qPCR) shows expression of myofibroblasts markers *Acta2*, *Tagln* and *Fnl1* in cultured BMSCs upon treatment with recombinant TGF β 1, endothelin 1 (ET1) or adrenomedullin (ADM). ($n = 3$). Data in graphs are presented as mean \pm SEM. P values, statistical analysis performed using the Mann-Whitney test (two-tailed)). n = independent biological samples.



Extended Data Fig. 10 | See next page for caption.

Extended Data Fig. 10 | *Lats2* and SRF control EC behavior. **a, b.** Representative confocal images of control and *Srf*^{ΔEC} femur show type H (EMCN^{high}, CD31^{high}) capillaries, Nuclei, DAPI (blue) (**a**) as well as PDGFRβ+ cells (red) and αSMA+ arterial SMCs (green) and EMCN (blue) in the femoral metaphysis (**b**). Graphs in (**b**) show quantification of vessel columns and arteries (n = 6). Data presented as mean ± SEM. P values, Mann–Whitney test (two-tailed). **c–e.** Confocal images showing ACAN+ (green) chondrocytes in femoral growth plate (gp) (**c**) and OSX+ cells (green) (**d**). μCT images of trabecular bone of *Srf*^{ΔEC} mutant and control (**e**) and quantitation of trabecular (tb) volume (BV/TV, bone volume/total volume) tb number and gp length (n = 6). Data presented as mean ± SEM. P values, Mann–Whitney test (two-tailed). **f, g.** Longitudinal tile scan confocal images showing EMCN+ (red) CD31+ (green) vessels in control, *Lats2*^{ΔEC} and *Lats2*

Srf^{ΔEC} compound mutant femur (**f**). Metaphysis (mp), growth plate (gp, dashed lines) and bone marrow (bm) are indicated. Quantification shows increase in CD31+ EMCN- area in *Lats2*^{ΔEC} metaphysis and rescue by inactivation of *Srf* (**g**) (n = 4). Data presented as mean ± SEM. P values, Tukey multiple comparison test (one-way Anova). **h.** Representative images showing OSX+ cells in control, *Lats2*^{ΔEC}, and *Lats2Srf*^{ΔEC} compound mutant femur. **i, j.** Representative μCT images of femoral trabecular bone (**i**). Quantitative analysis of trabecular bone (tb) thickness and separation (**j**) (n = 4). Data presented as mean ± SEM. P values, Tukey multiple comparison test (one-way Anova). **k.** Proposed model of YAP1/TAZ-induced endothelial-to-mesenchymal transition (EndMT) as a driver of myelofibrosis and osteosclerosis. n = independent biological samples. Created with [BioRender.com](https://www.biorender.com).

Reporting Summary

Nature Portfolio wishes to improve the reproducibility of the work that we publish. This form provides structure for consistency and transparency in reporting. For further information on Nature Portfolio policies, see our [Editorial Policies](#) and the [Editorial Policy Checklist](#).

Statistics

For all statistical analyses, confirm that the following items are present in the figure legend, table legend, main text, or Methods section.

- | | |
|-------------------------------------|--|
| n/a | Confirmed |
| <input type="checkbox"/> | <input checked="" type="checkbox"/> The exact sample size (n) for each experimental group/condition, given as a discrete number and unit of measurement |
| <input type="checkbox"/> | <input checked="" type="checkbox"/> A statement on whether measurements were taken from distinct samples or whether the same sample was measured repeatedly |
| <input type="checkbox"/> | <input checked="" type="checkbox"/> The statistical test(s) used AND whether they are one- or two-sided
<i>Only common tests should be described solely by name; describe more complex techniques in the Methods section.</i> |
| <input type="checkbox"/> | <input checked="" type="checkbox"/> A description of all covariates tested |
| <input type="checkbox"/> | <input checked="" type="checkbox"/> A description of any assumptions or corrections, such as tests of normality and adjustment for multiple comparisons |
| <input type="checkbox"/> | <input checked="" type="checkbox"/> A full description of the statistical parameters including central tendency (e.g. means) or other basic estimates (e.g. regression coefficient) AND variation (e.g. standard deviation) or associated estimates of uncertainty (e.g. confidence intervals) |
| <input type="checkbox"/> | <input checked="" type="checkbox"/> For null hypothesis testing, the test statistic (e.g. F , t , r) with confidence intervals, effect sizes, degrees of freedom and P value noted
<i>Give P values as exact values whenever suitable.</i> |
| <input checked="" type="checkbox"/> | <input type="checkbox"/> For Bayesian analysis, information on the choice of priors and Markov chain Monte Carlo settings |
| <input checked="" type="checkbox"/> | <input type="checkbox"/> For hierarchical and complex designs, identification of the appropriate level for tests and full reporting of outcomes |
| <input checked="" type="checkbox"/> | <input type="checkbox"/> Estimates of effect sizes (e.g. Cohen's d , Pearson's r), indicating how they were calculated |

Our web collection on [statistics for biologists](#) contains articles on many of the points above.

Software and code

Policy information about [availability of computer code](#)

- | | |
|-----------------|--|
| Data collection | RNA sequencing by NestSeq500, MiSeq (Illumina); Confocal immunofluorescence image were collected from leica TCS-SP8; Cell sorting and analyzed by FACS Aria II cell sorter (BD Bioscience); GraphPad Prism (version 9). Adobe Photoshop 2021 and Adobe illustrator 2021. |
| Data analysis | Data analysis and statistical tests were done using GraphPad Prism (Version 9). Confocal images were analyzed with Volocity 6.3 (Quorum Techonology) or imageJ(Version:2.0.0-re-69/1.52p). For FACS data analysis, we used FACSDiva v8.02 and flowjo.v10.

Single cell RNA sequencing data analysis
Raw sequencing data was converted to fast format using bcl2fastq (version 2.20.0.422). Sequencing reads were processed with cutadapt (version 3.5) and aligned and counted with STAR (version 2.7.10a). All further analyses were conducted with custom code and using existing modules, mainly matplotlib (version 3.5.3), Ann Data (version 0.8.0), scanpy (version 1.9.1), harmony (0.0.9), scran (version 1.24.1), scDblFinder (version 1.11.4), DESeq2 (version 1.36), igraph (version 0.10.4), sklearn (version 1.1.2), statsmodels (version 0.13.1), scipy (version 1.9.1), milopy (version 0.1.0) and slingshot (2.6.0). The major programming languages used were R (version 4.2.1) and python (version 3.8.10). Also the iRegulon plugin to Cytoscape was used (version 3.9.1). All code used to produce the computational analysis results and figures in this publication are available at https://gitlab.gwdg.de/pmajev/sivaraj_majev_lats2_ecs (10.5281/zenodo.11456485). |

For manuscripts utilizing custom algorithms or software that are central to the research but not yet described in published literature, software must be made available to editors and reviewers. We strongly encourage code deposition in a community repository (e.g. GitHub). See the Nature Portfolio [guidelines for submitting code & software](#) for further information.

Data

Policy information about [availability of data](#)

All manuscripts must include a [data availability statement](#). This statement should provide the following information, where applicable:

- Accession codes, unique identifiers, or web links for publicly available datasets
- A description of any restrictions on data availability
- For clinical datasets or third party data, please ensure that the statement adheres to our [policy](#)

Data availability

The scRNA-seq data generated in this study have been deposited in the gene expression omnibus (GEO) database under the accession number GSE225429 (<https://www.ncbi.nlm.nih.gov/geo/query/acc.cgi?acc=GSE225429>). The mouse reference genome GRCm39 with Gencode M26 annotation (https://www.gencodegenes.org/mouse/release_M26.html) was used for mapping the reads to in this study. All other relevant data supporting the key findings of this study are available within the article and its Supplementary Information files or from the corresponding author upon reasonable request.

Code availability

All code used to produce the computational analysis results and figures in this publication are available at https://gitlab.gwdg.de/pmajev/sivaraj_sivaraj_lats2_ecs. The assigned DOI is 10.5281/zenodo.11456485 (<https://doi.org/10.5281/zenodo.11456485>).

Human research participants

Policy information about [studies involving human research participants and Sex and Gender in Research](#).

Reporting on sex and gender

Population characteristics

Recruitment

Ethics oversight

Note that full information on the approval of the study protocol must also be provided in the manuscript.

Field-specific reporting

Please select the one below that is the best fit for your research. If you are not sure, read the appropriate sections before making your selection.

Life sciences Behavioural & social sciences Ecological, evolutionary & environmental sciences

For a reference copy of the document with all sections, see [nature.com/documents/nr-reporting-summary-flat.pdf](https://www.nature.com/documents/nr-reporting-summary-flat.pdf)

Life sciences study design

All studies must disclose on these points even when the disclosure is negative.

Sample size

No specific statistical methods were used to predetermine sample size. Sample size were chosen based on previous experience. (ref. kusumbe et al. Nature 2014; Ramasamy et al., Nature 2014; Sivaraj et al., Elife 2020; Sivaraj et al., Cell Report 2021).

Data exclusions

Cells are excluded in the single cell RNA-seq data. Cells with less than 1000 UMI or 800 features (>0 counts per feature) detected, were discarded. Similarly, only cells with less than 15% of counts stemming from mitotic genes or 5% from hemoglobin genes were retained. By these strict thresholds mostly remaining cells of the haematopoietic lineage and low quality cells were removed. Repeating the analysis without these cut-offs revealed no additional desired cell types. Only features present with more than 10 counts total from at least 10 cells were kept.

Replication

scRNA-seq experiments were performed in duplicates and other all experiments were repeated at least three times and performed independently to ensure reproducibility. All the attempts of replication experiments were successful.

Randomization

No formal method of randomization was used. All experiments involving wildtype mice were performed on inbred C57Bl6 strain with male mice of same age group. For mutant studies we used both male and female of same age group, and phenotype were always compared between same age and sex of animals. For Fibrosis model we used age and sex matched mice.

Blinding

When appropriate, data analysis was done in a blinded manner before being unblinded once the analyses were finished.

Reporting for specific materials, systems and methods

We require information from authors about some types of materials, experimental systems and methods used in many studies. Here, indicate whether each material, system or method listed is relevant to your study. If you are not sure if a list item applies to your research, read the appropriate section before selecting a response.

Materials & experimental systems

n/a	Involved in the study
<input type="checkbox"/>	<input checked="" type="checkbox"/> Antibodies
<input checked="" type="checkbox"/>	<input type="checkbox"/> Eukaryotic cell lines
<input checked="" type="checkbox"/>	<input type="checkbox"/> Palaeontology and archaeology
<input type="checkbox"/>	<input checked="" type="checkbox"/> Animals and other organisms
<input checked="" type="checkbox"/>	<input type="checkbox"/> Clinical data
<input checked="" type="checkbox"/>	<input type="checkbox"/> Dual use research of concern

Methods

n/a	Involved in the study
<input checked="" type="checkbox"/>	<input type="checkbox"/> ChIP-seq
<input type="checkbox"/>	<input checked="" type="checkbox"/> Flow cytometry
<input checked="" type="checkbox"/>	<input type="checkbox"/> MRI-based neuroimaging

Antibodies

Antibodies used

All antibody details (clone and manufacturer) are included in methods and also listed below:
 Antibody Manufacturer Catalog number Concentration
 Rat monoclonal anti-Endomucin (V.7C7) (Santa Cruz, Cat# sc-65495, 1:100 dilution),
 Goat polyclonal anti-CD31 (R&D, Cat# AF3628, 1:100 dilution),
 Rabbit-polyclonal anti-Fabp5 (Lifespan Bioscience, Cat#C312991, 1:100 dilution),
 Goat anti-PDGFRβ (R&D, Cat# AF1042, 1:100 dilution),
 Mouse monoclonal alpha-smooth muscle actin-Cy3 (Sigma, Cat#C6198, 1:200 dilution),
 Mouse monoclonal alpha-smooth muscle actin-eFluor660 (eBioscience, Cat#50-9760-82, 1:200 dilution),
 Rabbit monoclonal anti-Yap1/Taz (D24E4, Cell signaling, Cat#8418, 1:100 dilution),
 Rabbit monoclonal anti-Vimentin (D21H3, Cell signaling, Cat#5741, 1:100 dilution),
 Rabbit polyclonal anti-Tagln (Sm22a, Abcam, Cat#ab14106, 1:100 dilution),
 Rabbit polyclonal anti-Fibronectin (Fn1, Sigma, Cat#F3648, 1:100 dilution),
 Rabbit polyclonal anti-Thrombospondin 1 (Thbs1, Abcam, Cat#ab85762, 1:100 dilution),
 Rabbit polyclonal anti-Angpt2 (Abcam, Car# ab8452, 1:100 dilution),
 Rabbit polyclonal anti-Cav1 (Cell signaling, Cat#3238, 1:100 dilution),
 Rabbit polyclonal anti-Col-I (Millipore, Cat#AB765P, 1:100 dilution),
 Rabbit polyclonal anti-Col-X (Abcam, Cat#ab58632, 1:100 dilution),
 Rabbit polyclonal anti-LATS2 (GeneTex, Cat#GTX87529, 1:50 dilution),
 Rabbit polyclonal anti-Col4 (AbD Serotec, Cat# 2150-1470, 1:100 dilution),
 Rabbit-polyclonal anti-Osterix (Abcam, Cat#ab22552, 1:300 dilution),
 Roat polyclonal anti-Mmp9 (R&D, Cat#AF909, 1:200 dilution),
 Rabbit polyclonal anti-Aggregan (Millipore, Cat#AB1031, 1:100 dilution),
 Rabbit anti-vATPaseB1/B2 (Abcam, Cat#200839, 1:100 dilution),
 Rat anti-mouse Ter119 (BD Bioscience, Cat#553673, 1:200 dilution),
 Rat anti-mouse B220 (BD Bioscience, Cat#553090, 1:200 dilution),
 Rat-monoclonal anti-active Itgb1 (BD Bioscience, Cat#553715, 1:50 dilution),
 Rabbit polyclonal anti-FAK (pY397) (ThermoFisher, Cat#44-624G, 1:50 dilution),
 Rabbit monoclonal anti-Runx2 (Abcam, Cat#ab192256, 1:200 dilution),
 Rat monoclonal anti-Srf (from Alfred Nordheim, 1:50 dilution),
 lineage cell detection cocktail-biotin (Miltenyi Biotec, Cat#130-092-613, 1:100 dilution),
 Rat monoclonal anti-Ly6A-PE-cy7 (BD Pharmingen, clone D7, Cat# 558162, 1:100 dilution),
 Rat monoclonal anti-CD117-APC (BD Pharmingen, clone 2B8, Cat# 553356, 1:100 dilution),
 Hamster monoclonal anti-CD3e-FITC eBioscience, clone 145-2C11, Cat# 11-0031, 1:100 dilution),
 Rat monoclonal anti-B220-APC (Invitrogen, RA3-6B2, Cat# RM2605, 1:100 dilution),
 Rat monoclonal anti-CD11b-APC (Biolegend, M1/70, Cat# 101212, 1:100 dilution),
 Rat monoclonal anti-Ly-6G(Gr-1)-BV605 (Biolegend, RB6-8C5, Cat# 108440, 1:100 dilution),
 Rat monoclonal anti-CD45-PE (BD Pharmingen, 30-F11, Cat# 553081, 1:100 dilution),
 Rat monoclonal anti-TER-119-APC (eBioscience, Cat# 17-5921, 1:100 dilution),
 Rat monoclonal anti-CD41-BV605 (Biolegend, MWReg30, Cat# 133921, 1:100 dilution)
 Alexa Fluor 488 (Thermo Fischer Scientific, Cat#A21208, 1:100 dilution)
 Alexa Fluor 546 (Thermo Fischer Scientific, Cat#A11056, 1:100 dilution)
 Alexa Fluor 594 (Thermo Fischer Scientific, Cat#A21209, 1:100 dilution)
 Alexa Fluor 647 (Thermo Fischer Scientific, Cat#A31573 or Cat#A21447, 1:100 dilution)
 Phalloidin -488 (Invitrogen, Cat# A12379, 1:100 dilution)

Validation

All antibodies used in the study have been commercially available and previously used by our group (ref. kusumbe et al. Nature 2014; Ramasamy et al., Nature 2014; Sivaraj et al., Elife 2020; Sivaraj et al., Cell Report 2021). The complete information and all validation information for each Ab as well as previous publications that have used each Ab can be found on the manufacturer's website.

Animals and other research organisms

Policy information about [studies involving animals](#); [ARRIVE guidelines](#) recommended for reporting animal research, and [Sex and Gender in Research](#)

Laboratory animals

All animals used in this study are *Mus musculus* species, C57/BL6 background strain independent of genotype. All mice were maintained in individually ventilated cages (IVC), with constant access to food and water under a 12 h light and 12 h dark cycle regime. Air flow, temperature (21–22 °C) and humidity (55–60%) were controlled by an air management system. Animals were checked daily and maintained in specific pathogen-free (SPF) conditions. Sufficient nesting material and environmental enrichment was provided.

Transgenic mice were generated from our laboratory, *Cdh5*(PAC)-CreERT2, *Yap1* mice; *Yap1/Taz* flox/flox mice from Helen McNeill Laboratory; *Lats2* flox/flox from Dae-Sik Lim Laboratory, KAIST, Korea; *Srf* flox/flox mice from Alfred Nordheim; and following transgenic mice *Rosa26-mTG* were purchased from Jackson Laboratory. 12-week old male and female transgenic mice were used for most of the experiments.

For mutant experiment, mice were bred to *Cdh5*(PAC)Cre-ERT2 to generate inducible mouse model. Cre negative were used as litter mate control. Most of the experiments were performed at 12 weeks.

Fibrosis ThPO mouse experiment were performed on 10-12 weeks-old mice and analyzed in 8 - 10 weeks later.

Wild animals

No wild animals were used in the study.

Reporting on sex

Male and female mice were used for most of the experiments.

Field-collected samples

No field collected samples were used.

Ethics oversight

All animal experiments were performed according to the international guidelines and laws, approved by local animal ethical committee University of Muenster and Max Planck Institute for Molecular Biomedicine with permissions granted by the Landesamt für Natur, Umwelt und Verbraucherschutz (LANUV) of North Rhine-Westphalia, Germany.

ThPO and MPLW515L bone fibrosis studies were conducted according to protocols approved by the Central Animal Committee (Centrale Commissie Dierproeven [CCD], Netherlands) in accordance with legislation in The Netherlands.

Note that full information on the approval of the study protocol must also be provided in the manuscript.

Flow Cytometry

Plots

Confirm that:

- The axis labels state the marker and fluorochrome used (e.g. CD4-FITC).
- The axis scales are clearly visible. Include numbers along axes only for bottom left plot of group (a 'group' is an analysis of identical markers).
- All plots are contour plots with outliers or pseudocolor plots.
- A numerical value for number of cells or percentage (with statistics) is provided.

Methodology

Sample preparation

Bone marrow (BM) isolation was performed using crushing methodology, followed by MACS beads and quadromacs (LS columns) were used for lineage depletion or bone marrow stromal cells enrichment. We used femur and tibia are separated by surgical dissection and bone marrow were collected. Bones were dissected into small size and digested with Collagenase for 30 min at 37°C. Cells were washed with 1%BSA and filtered to obtained a single cell suspension. The detailed BM isolation protocol is included in the methods section.

Instrument

FACS Aria II cell sorter (BD Bioscience)

Software

FACSDiva (BD Bioscience) was used for sorting and analysis.

Cell population abundance

Sorted cell quality were analysed by confocal microscopy.

Gating strategy

Single viable cells were gated initially forward and side scatter.

- Tick this box to confirm that a figure exemplifying the gating strategy is provided in the Supplementary Information.